UNIVERSITY OF CALIFORNIA,
IRVINE

Controlling the Wetting Behaviors of Copper Nanostructures through Solution Immersion Method

THESIS

submitted in partial satisfaction of the requirements
for the degree of

MASTER OF SCIENCE

in Materials Science and Engineering

by

Pranav P. Dubey

Thesis Committee:
Assistant Professor Yoonjin Won, Chair
Associate Professor Ali Mohraz
Assistant Professor Allon Hochbaum

2017

DEDICATION

To

my parents and friends

in recognition of their worth

an apology

Our virtues and our failings are inseparable, like force and matter. When they separate, man is no more.

Nikola Tesla
The Problem of Increasing Human Energy

and hope

Truth is like a vast tree, which yields more and more fruit, the more you nurture it.

Mahatma Gandhi
The Story of My Experiments with Truth

TABLE OF CONTENTS

LIST OF FIGURES

LIST OF TABLES

ACKNOWLEDGEMENTS

I would like to express my heartfelt gratitude to my thesis committee chair-Professor Yoonjin Won, whose curious outlook and brilliant mind convincingly persuaded me in seeking greater depths regarding research and scholarship, and an excitement about teaching. Without her counsel and persistent aid, this thesis would not have been possible.

I would also like to thank Dr. Qiyin Lin for training me well in performing comprehensive materials characterization with the scanning electron microscopy and the X-ray diffraction spectroscopy techniques without which this research would not have found its purpose. I also appreciate the valuable reviews from my thesis committee members – Dr. Ali Mohraz and Dr. Allon Hochbaum.

I would like to acknowledge my lab mates, Quang Pham, Kush Thukral and Mario Soler for their key assistance in fabricating the copper inverse opal samples, polishing copper plates, acquiring contact angles and productive suggestions during group meetings.

Finally, I am grateful to the Irvine Materials Research Institute for letting me work with the Phillips XL-30 Scanning Electron Microscope and the Rigaku Smartlab X-Ray Diffractometer. This work was sponsored by the Samsung Global Research Outreach Program and the School of Engineering at the University of California at Irvine (UC Irvine).

ABSTRACT OF THE THESIS

Controlling the Wetting Behaviors of Copper Nanostructures through Solution Immersion Method

By

Pranav Dubey

Master of Science in Materials Science and Engineering

University of California, Irvine, 2017

Assistant Professor Yoonjin Won Irvine, Chair

Addressing a desired surface wettability has been a significant challenge for a variety of innovative thermofluidic applications from anti-icing coating to two-phase heat exchangers. Surface wettability can be controlled by fabricating nanostructures on the surfaces and modifying their chemistry. While numerous nanofabrication efforts have been investigated for this purpose, a solution immersion method is suggested in this research since it can effectively install nanostructures on two-dimensional or three-dimensional surfaces over a large area. Therefore, we employ the solution immersion method in order to investigate the wettability of copper oxide nanostructures related to fabrication parameters. The examples of copper oxide nanostructures include nanoneedles and nanoflowers/nanograsses on polished copper substrates and open-cell porous copper structures (i.e. copper inverse opals). Detailed analysis is followed to quantify surface structural details, chemical composition, and surface wettability. The understanding of structure- and chemistry-dependent wettability will pave the way for the implementation of copper nanostructures with well-controlled wetting properties into future copper-based thermofluidic applications such as heat exchangers and heat pipes.

CHAPTER 1: INTRODUCTION

The design of metamaterials has attracted significant attention owing to their unique combinations of specific surface area, transport physics, and interfacial physics, enabling a wide range of applications such as sensors[1], water-harvesting surfaces[2], and thermofluidic devices[3]. In particular, for thermofluidic applications, controlling surface wetting characteristics via surface treatment methods is interesting to improve liquid transport through the void fraction of metamaterials. Despite several efforts in past, the development of a facile and economical surface treatment methods with accurate control of wetting characteristics still remains a challenge. A solution immersion technique that creates nanostructures on surfaces has a potential to efficiently tune the surface wetting behaviors by modulating both the chemistry and morphological details of nanostructures. Therefore, we investigate the effects of various types of nanostructures by employing solution immersion methods with the aim of optimizing wetting characteristics in this study.

1.1 Demonstration of Nanostructures on a Flat Substrate

In recent years, the control of wetting characteristics of solid surfaces has resurfaced as a topic impacting many fields of science and technology such as anti-icing[4], anti-biofouling[5], anti-corrosion[6], self-cleaning[7], and microfluidics system[2]. The wetting behaviors of a surface can be modified based on two basic approaches: (1) The first approach is to create structural roughness on intrinsically hydrophobic or hydrophilic surfaces. (2) The second approach is to modify surfaces with low or high surface energy materials[8].

Typically, a surface is defined to be hydrophobic if the contact angle (CA) is $>90^{o}$ and hydrophilic if the CA is $<90^{o}$. Furthermore, a surface is superhydrophobic if the CA is $>150^{o}$ and

superhydrophilic if the CA is <10°. Traditional theories such as Young's model (figure 1.1)[9], Wenzel's model[10], and Cassie-Baxter's model[11] explain interfacial physics as a function of fluid properties and surface roughness. The Young's model demonstrates the dependence of surface wettability on surface tensions at three contact interfaces (*i.e.* solid-vapor, solid-liquid, and liquid-vapor interface). The classic Young-Dupre's equation is given as:

$$cos\theta = \frac{\gamma_{SV} - \gamma_{SL}}{\gamma_{LV}} \quad \ldots 1.1$$

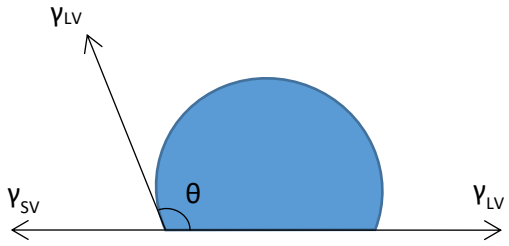

Figure 1.1 Surface tensions on a water droplet on a smooth surface.

where θ is the CA; γ_{SV}, γ_{SL}, and γ_{LV} are the surface tensions at the solid-vapor, solid-liquid, and liquid-vapor interface, respectively. However, the Young's model considers only surface tensions but neglects surface roughness on CAs.

Wenzel's equation, thereby, explains CAs on rough surfaces (figure 1.2a) associated with a roughness factor r (ratio of actual surface area to projected surface area),

$$cos\theta^* = rcos\theta \quad \ldots 1.2$$

where θ^* is the apparent CA on the rough surface, and θ is the CA on a smooth surface with identical surface chemical composition. Equation 1.2 can be rearranged as

$$\theta^* = \cos^{-1}(r\cos\theta)$$

where θ^* is inversely proportional to r for $0 < \theta < 90^o$, and directly proportional to r for $90^o < \theta < 180^o$. This suggests that an increase in roughness increases the hydrophilicity of a formerly hydrophilic surface and the hydrophobicity of a formerly hydrophobic surface. For a significantly large value of r, the term $rcos\theta$ is greater than 1. Since $cos\theta^*$ is always ≤1 the Wenzel's model is only valid for low or moderately rough surfaces such that $rcos\theta \leq 1$.

Another approach to explain CAs on rough surfaces is the Cassie-Baxter model that modified the equation 1.3 for surfaces with a broad range of roughness by considering the surface to be a composite of air and solid (figures 1.2b and c)

$$cos\theta^* = f_1 cos\theta_1 + f_2 cos\theta_2 \quad \ldots 1.3$$

where f_1 is the fraction of liquid-solid interface, f_2 is the fraction of the liquid-air interface, θ_1 is the CA on a solid surface, and θ_2 is the CA on air surface. This equation suggests that the presence of air pockets underneath a rough nanostructure increases the CA and hence causes the surface to become more hydrophobic. The above equations are only valid when the water droplet size is of the order of nanoliter to neglect the gravity effect and two orders of magnitude higher than the wavelength of roughness[12,13] to approach the most stable CA (with negligible evaporation).

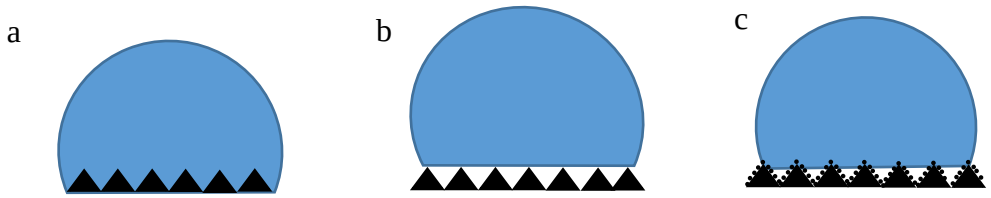

Figure 1.2 Different states of wetted rough surfaces: (a) Wenzel's state, (b) Cassie's superhydrophobic state, and (c) Cassie's state of partial wetting on nanostructured structures.

1.2 Fabrication Methods to Demonstrate Nanostructures on a Metal Substrate

Numerous methods to fabricate nanostructures on metal substrates have been explored in the past. Those fabrication methods include sandblasting and fluorinated lubricant infiltration[14], plasma treatment[15], hydrothermal methods[16], spin-coating methods[17], self-assembly techniques[18], screen-printing techniques[19], electrochemical process[20], solution immersion methods[21,22,7], and a combination of two or more methods[23,8]. Many of these processes are subject to limitations by severe conditions (high fabrication temperature or pressure), fabrication complexity, and expensive costs. The solution immersion method is a one-step process by which we can accurately

control the nanostructure morphology by varying process parameters. In this method, a clean substrate is immersed in a basic solution to cause a controlled surface oxidation. A variety of nanostructures can be created by varying solution composition, immersion time, and solution temperature. In particular, the design of copper nanostructures has been interesting in many applications as copper is widely used in industry[1,2]. As a result, various copper oxide nanostructures have been availble as lised in table 1.1, which exhibit a wide range of wetting characteristics (from hydrophobic to hydropihlic) with varying fabrication parameters.

Table 1.1 Various copper oxide nanostructures by solution immersion methods and their corresponding chemical compositions, characteristic lengths, water contact angles, and total fabrication time.

Morphology	**Chemical composition**	**Characteristic length (μm)**	**Contact angle (deg)**	**Fabrication time (mins)**
Nanoneedles[24]	Cu_2O	0.2	20	5
	CuO	1.5	9	5
Nanoribbon arrays[25]	$Cu(OH)_2$	100	4.2	10
Nanowires[26]	CuO	0.1	9	15
Microflowers with nanorod arrays[27]	$CuO/Cu(OH)_2$	4	5	30
Dandelion and sheet like structure[28]	CuO	2.5	158	40
Nano crystals[29]	CuO	3	0	80
Coralline like nanospheres[30]	$CuO\text{-}Cu_3Pt/Cu$	0.12	130	100
		0.2	170	100
Hierarchical spheres and flowers[31]	CuO	2.3	50	120
Flower like clusters[22]	$Cu(CH_3(CH_2)12COO)_2$	51.66367	70	4320
		59.868	125	
		98.88175	162	
Microcabbages[32]	CuO	0.09	9	8640
Nanoflower film[33]	Cu_2O	6	120	21600
Sheet like nanograins with nanogrooves[34]	CuO	5	54	43200
Nanotube arrays[35]	$Cu(OH)_2$	0.35	11.5	72000

1.3 Demonstration of Nanostructures using Copper Oxidation Process

In general, the solution immersion method involves chemical oxidization of metal surfaces to form metal oxide nanostructures with unique morphologies. With copper substrates, the nanostructures are predominantly composed of CuO, so it is important to understand the mechanism of formation of the oxides from base copper.

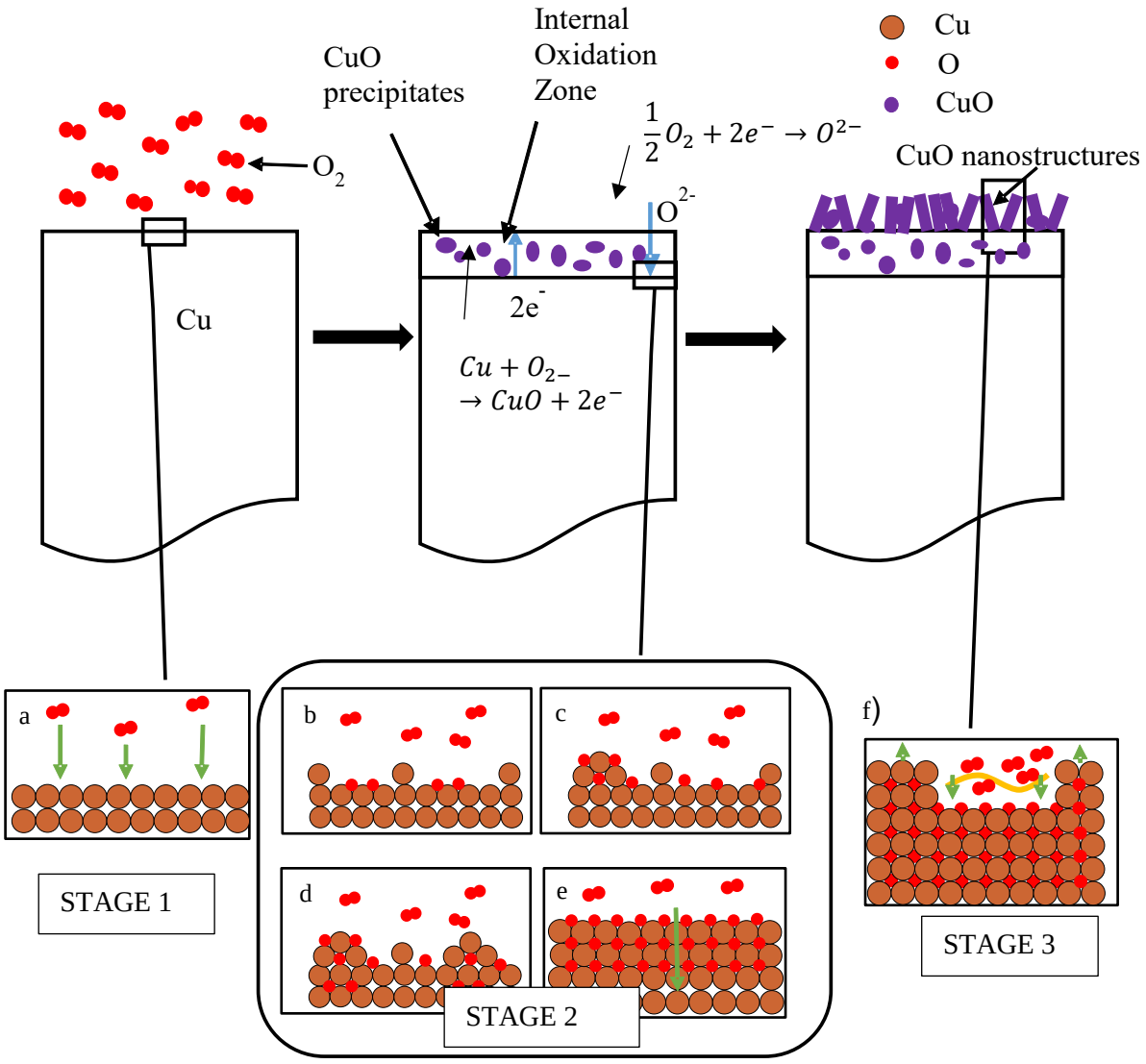

Figure 1.3 Schematic diagram showing the mechanism of copper oxidation. (a) Oxygen atoms approach the copper surface, (b-e) copper atoms reconstruct as the initial oxide forms an IOZ, and (f) finally a nonuniform oxide layer develops on the surface.

The oxidation of copper surface for the formation of nanostructures occurs in three steps as explained below[38,39]:

STAGE 1: Dissolution of oxygen into the surface layer (lattice of Cu) (figure 1.4a).

STAGE 2: Formation of an Internal Oxidation Zone (IOZ) involves the following steps

2.1.Cu surface oxidizes to form CuO nuclei (figure 1.4b).

2.2.CuO precipitates start to grow on the surface (figure 1.4c).

2.3.A concentration gradient develops across the IOZ (figure 1.4d).

2.4.Oxygen atoms diffuse inwards extending the oxide particles (figure 1.4e)

STAGE 3: Development of non-uniform CuO layer (figure 1.4f)

3.1. Diffusion of Cu atoms in the oxide layer is slower than the flow of oxygen atoms towards the copper surface because a highly basic solution quickly furnishes oxygen atoms to the surface whereas Cu faces obstacles to diffuse through the IOZ.

3.2. Oxide builds up at IOZ-oxides interface and pushes up.

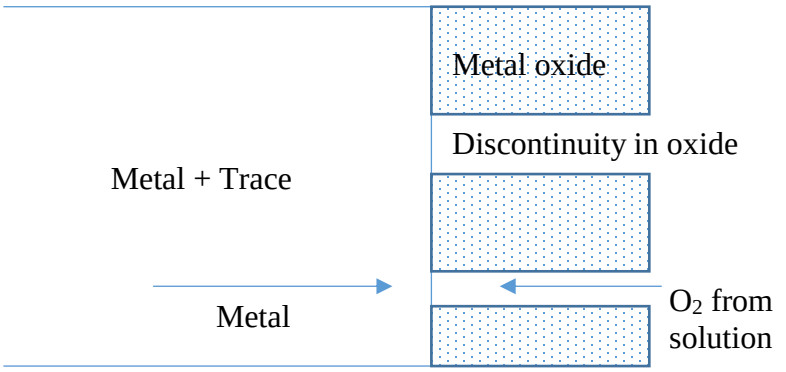

Figure 1.4 Non-uniform oxide layer of metal leading to oxide-nanostructure formation where the metal is copper in this study[40].

Before the formation of nanostructures of copper oxides, the metal oxides form an incoherent surface layer. The discontinuities shown in figure 1.5 may comprise of pores, cracks, or channels of any shape, obviously possessing little protective action on the underlying metal surface[37]. Such discontinuities act as nucleation sites for the formation of nanostructures.

The "internal oxidation zone" (IOZ) is formed when the diffusivity of oxygen (D_O) is larger than that of metal (D_M) and comprises of sub-surface oxides formed when oxygen penetrates deep into the metal surface. If the partial pressure of oxygen in the solution is high enough, external oxides start forming by precipitation of latest oxide particles at the border of IOZ[40].

According to the classical theory of nucleation, the activation barrier to nucleation (G^*) can be estimated from the free-energy change for the formation of a nucleus of radius R:

$$\Delta G = 4\pi r^2\sigma + \left(\frac{4}{3\pi R^3}\right)(\Delta G_v + \Delta G_S) \quad \dots 1.4^{40}$$

where σ is the specific interfacial free energy, ΔG_v is the free energy change per unit volume of those precipitated particles formed during reaction, and ΔG_S is the specific strain energy. The mechanism of nucleation and initial growth of oxide islands on a clean Cu surface has been proposed in terms of "capture zones"[39]. Aggregation and contribution to island growth will be preferred over nucleation of new islands when oxygen atoms land in these capture zone. The saturation number of islands that can act as nucleation sites, N_{sat}, is expressed as

$$N_{sat} = \frac{\left(1 - e^{-kL_d^2T}\right)}{L_d^2} \quad \dots 1.5$$

where L_d is the radius of capture zone, k is the initial island nucleation rate, and T is time allowed for nucleation. This model is valid for oxidation of Cu (100) and Cu (110).

In summary, we discuss the importance of the nanoscale architectures' design and their impacts on the wetting behaviors, which can be explained by classic interfacial physics theories. We also discuss literature studies that utilize solution immersion methods to create various nanostructures on copper substrates and their resulting CAs. Since solution immersion methods involve copper oxidation, we investigate the oxidation mechanism that forms unique morphology of copper oxides.

CHAPTER 2: DESIGN OF COPPER OXIDE NANOSTRUCTURES

The solution immersion method is a facile and rapid technique to fabricate nanostructures on a copper surface by precisely controlling process parameters. In this chapter, we study nanostructuring processes on a bare copper using solution immersion methods by varying parameters such as chemical composition, solution immersion time, and processing temperature.

2.1 General Fabrication Procedure for Solution Immersion Methods

The solution immersion method generally involves three steps to fabricate nanostructures on a copper surface, including (2.1.1) cutting and polishing, (2.1.2) cleaning, and (2.1.3) solution immersion and drying.

2.1.1 Cutting and Polishing

Copper plates are cut to size 1 cm x 1 cm for a solution immersion method. The samples are polished with 220, 320, 400, 500, 600, 800, 1000, and 1200 grits using water as a lubricant. Appropriate polishing is important to obtain a uniform surface for accurate repeatability of results. The SEM image of the unpolished copper sample (figure 2.1a) possesses significantly more scratches than the polished copper (figure 2.1b).

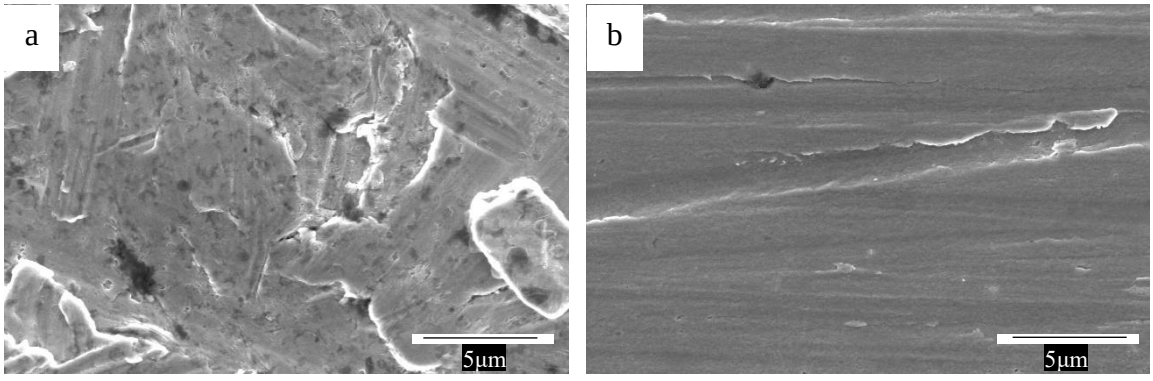

Figure 2.1 SEM images of (a) unpolished copper plate and (b) polished copper plate from 220 to 1200 grits.

2.1.2 Cleaning

The polished copper samples are rinsed for 10 mins in acetone ultrasonically, methanol (30 secs), isopropanol (30 secs), and deionized (DI) water (30 secs). Then samples are immersed in 2 M HCl solution to remove surface oxides after an air dry. Finally, the samples are washed with DI water, dried in air, and are ready for a solution immersion.

2.1.3 Solution Immersion and Drying

The cleaned samples are carefully immersed in an oxidizing solution with a tweezer for an amount of time decided by the fabrication plan. In general, two sets of solutions are prepared to observe various types of nanostructures.

- Solution A: $NaClO_2$, NaOH, $Na_3PO_4 \cdot 12H_2O$, and DI water,
- Solution B: NaOH, $K_2S_2O_8$, and DI water.

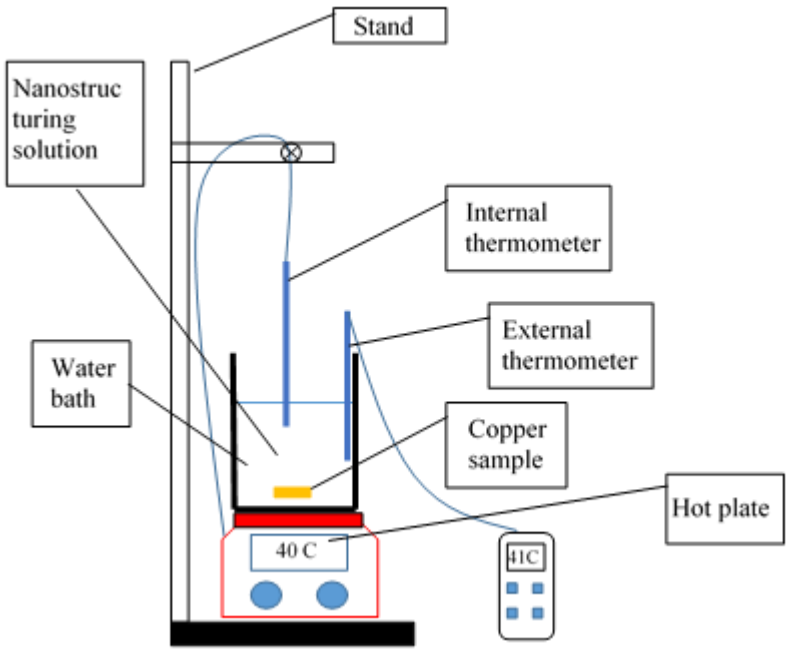

Figure 2.2 Fabrication setup for solution immersion shows a 1 cm x 1cm polished copper sample immersed in a chemical solution with an accurate control of the solution temperature.

Figure 2.2 illustrates the fabrication setup for the solution immersion method. The solution temperature is confirmed by using two thermometers - the hot plate's internal thermocouple and an external thermocouple. Finally, the samples are dried in air at room temperature.

2.2 Solution A - Nanoflakes

2.2.1 Control Parameters and Variation

To fabricate CuO nanoflakes, the solution composition and solution temperature are held at 3.75 gm $NaClO_2$, 5 gm NaOH and 10 gm $Na_3PO_4 \cdot 12H_2O$ in 100 ml DI water and 95 ^oC[34], respectively. The nanostructures' morphology remains as nanoflakes for immersion time from 1 min to 18 mins as presented in table 2.1. The density of nanoflakes is observed to increase with increasing immersion time as shown in figure 2.3a-d. The sparse nanoflakes form at 1 min

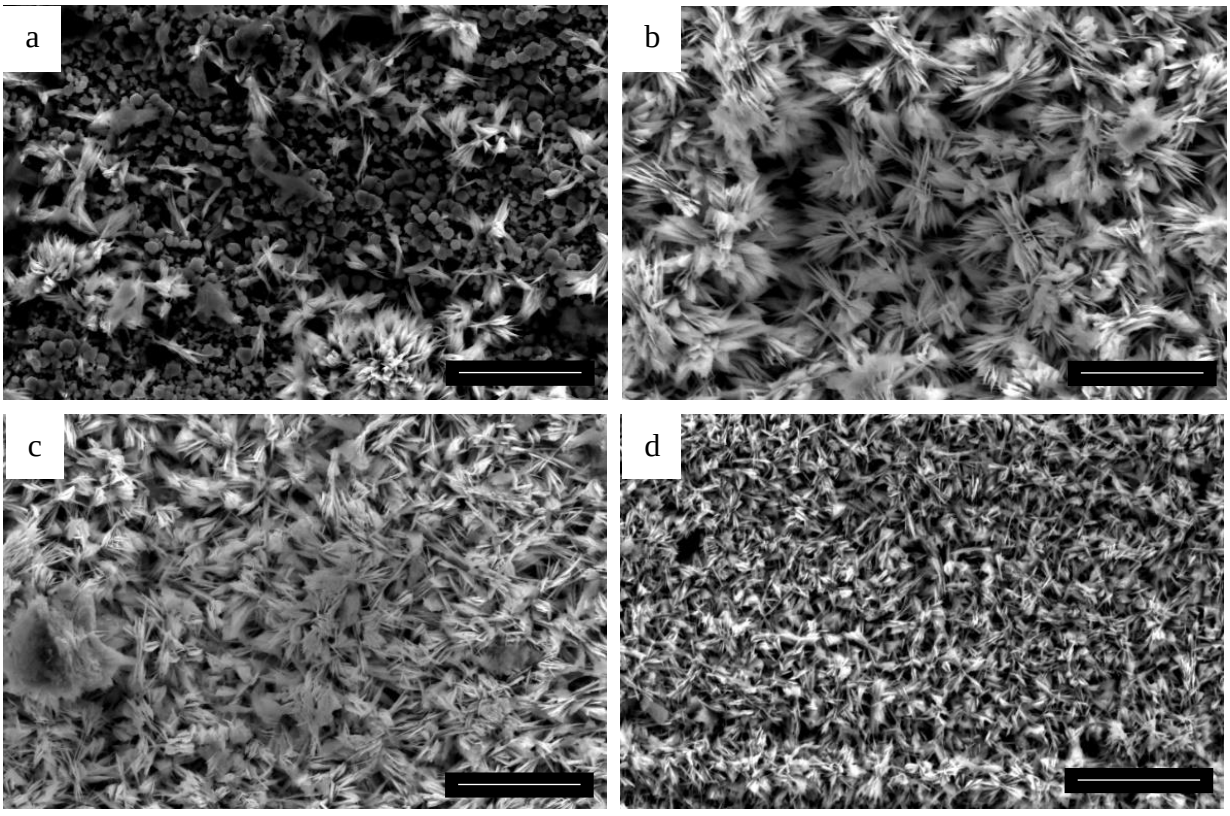

Figure 2.3 Nanoflakes fabricated on polished copper substrates by immersing in solution A for (a) 1 min, (b) 5 mins, (c) 10 mins, and (d) 18 mins (Scale bar=5μm)

immersion, rapidly increase in size (1 μm to 4 μm), and agglomerate up to 5 mins of immersion, as observed in figure 2.3b and figure 2.4. However, they dissociate as the immersion time is increased beyond 10 mins (figure 2.3c). We observe a clear reduction in the size of nanoflakes with an increase in immersion time to 18 mins (~1 μm) (figure 2.3d and figure 2.4).

Table 2.1 Nanostructure morphology at different immersion times for solution A.

Solution A	0.4 M $NaClO_2$, 1.25 M NaOH, 0.26 M $Na_3PO_4 \cdot 12H_2O$				
		Time (mins)			
		1	5	10	18
Temp (^oC)	95	Nanoflakes	Agglomerated nanoflakes	Nanoflakes	Nanoflakes

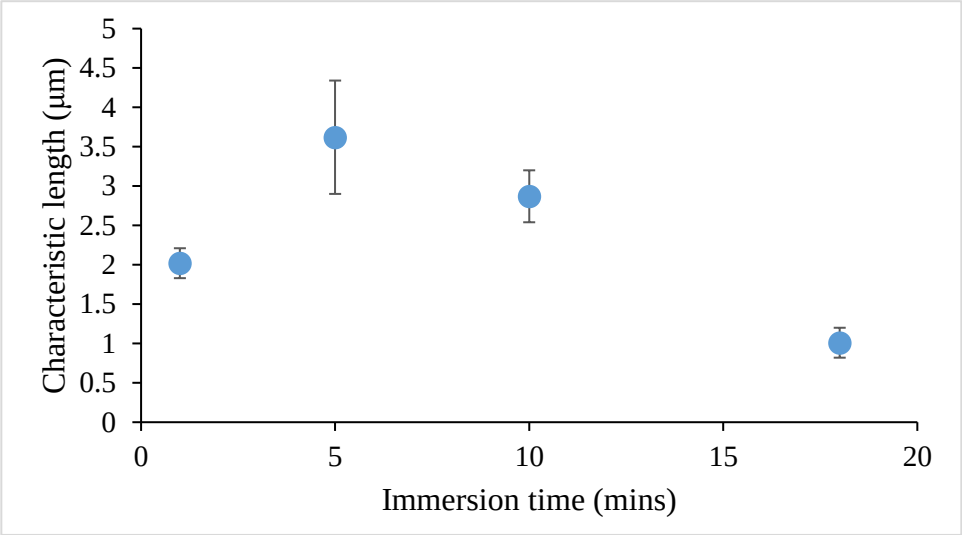

Figure 2.4 Characteristic length of nanoflakes with varying immersion time show an initial increase (agglomeration) followed by a gradual decrease (as the nanoflakes dissociate).

2.2.2 Wetting Characteristics

The surface wetting behaviors of fabricated nanostructures are measured using a contact angle meter (MCA-3 Kyowa Interface Science). As a result, figure 2.5 shows the change in CAs of nanoflakes with varying immersion time. With the increase in immersion time, the CA decreases from about 135^o to 110^o. On close observation, the CAs stay constant at ~135^o till 5 mins immersion beyond which there is a sudden dip to ~110^o. We suppose this occurs due to the

agglomeration of nanoflakes to form an astral shaped structure at 5 mins as observed in figure 2.3b.

The nanoflakes display a minor change in CAs with varying immersion time and lie in the hydrophobic regime. This motivates us to fabricate nanostructures possessing both hydrophobic and hydrophilic characteristics depending on the solution immersion time.

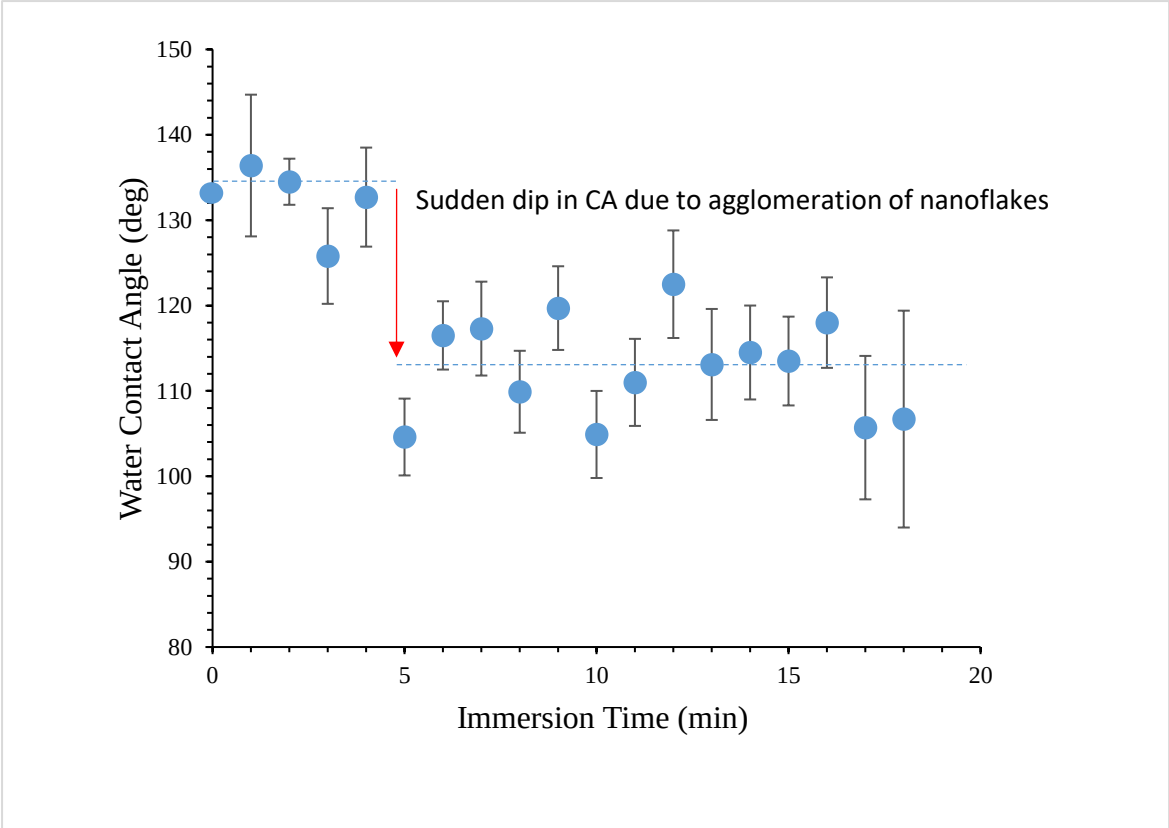

Figure 2.5 CA and droplet volume vs immersion time for nanoflakes fabricated with the solution immersion method (solution A).

2.3 Solution B - Nanoflowers/Nanograsses/Nanoneedles

Previous researchers observed that the solution B (NaOH, $K_2S_2O_8$) forms two-level nanoflowers/nanograsses with changing immersion time and solution concentration[35,36]. Although the creation of flower-based nanostructures has a potential to possess hydrophobicity because of multi-level hierarchy, the control of their wetting behaviors is yet to be addressed. The presented solution immersion method with solution B enables a direct control of nanostructure morphologies

by modifying process parameters including chemical composition and immersion time to modulate their surface wettability.

2.3.1 Control Parameters and Variation

A full-factorial fabrication plan is devised to observe various nanostructures at different immersion time, solution temperature, and solution concentration using solution B. As shown in table 2.2, we vary the solution temperature from 27ºC to 60ºC, the immersion time from 3 mins to 60 mins, and solution concentrations from B1 to B3 to observe their effects on the nanostructures'

Table 2.2 Full-factorial experiments showing various nanostructures fabricated with solution B at 84 different fabrication conditions.

Solution B1		0.1M $K_2S_2O_8$, 2M NaOH						
		Time (mins)						
		3	10	20	30	40	50	60
Temp (^{o}C)	27	NF+NG	NF+NG	NF+NG	NF+NG	NF+NG	NF+NG	NF+NG
	40	NF+NM	NF+NM	NF+NM	NF+NM	NF+NM	NF+NM	NF+NM
	50	SNN+NT	NN+NT	NN+NT	NN+NT	NN+NT	NN+NT	NN+NT
	60	SNN	SNN	SNN	SNN	SNN	SNN	SNN
Solution B2		0.05M $K_2S_2O_8$, 2M NaOH						
		Time (mins)						
		3	10	20	30	40	50	60
Temp (^{o}C)	27	NONE	NF+NG	NF+NG	NF+NG	NF+NG	NF+NG	NF+NG
	40	SNN+NF	NM	NM	NM	NM	NM	NM
	50	SNN	NM	NM	NM	NM	NM	NM
	60	LNN	LNN	LNN	LNN	LNN	LNN	LNN
Solution B3		0.1M $K_2S_2O_8$, 1M NaOH						
		Time (mins)						
		3	10	20	30	40	50	60
Temp (^{o}C)	27	SNF+NG	SNF+NG	SNF+NG	SNF	SNF	SNF	SNF
	40	SNF+NG	SNF+NN+NT	SNF+NN+NT	NN+NT	NN+NT	NN+NT	NN+NT
	50	SNN	SNN	SNN	SNN	SNN	SNN	SNN
	60	SNN	SNN	SNN	SNN	SNN	SNN	SNN

RNF-nanoflowers (3-4 μm); NG-nanograss (3-4 μm); SNN-small nanoneedles (~0.3 μm); LNN-large nanoneedles (~2 μm); NT-nanotrenches (3-4 μm); NM-nanomesh (0.3-0.5μm); SNF-spiky nanoflowers (3-4 μm).

size, shape, and hierarchy. The solution concentration is varied as 0.1M $K_2S_2O_8$ + 2M NaOH, 0.05M $K_2S_2O_8$ + 2M NaOH, and 0.1M $K_2S_2O_8$ +1M NaOH such that we note the effects of both NaOH and $K_2S_2O_8$ on the nanostructures with decreasing basicity. In general, with increasing solution temperature, there is a decrease in the hierarchy and overall surface nanostructure size.

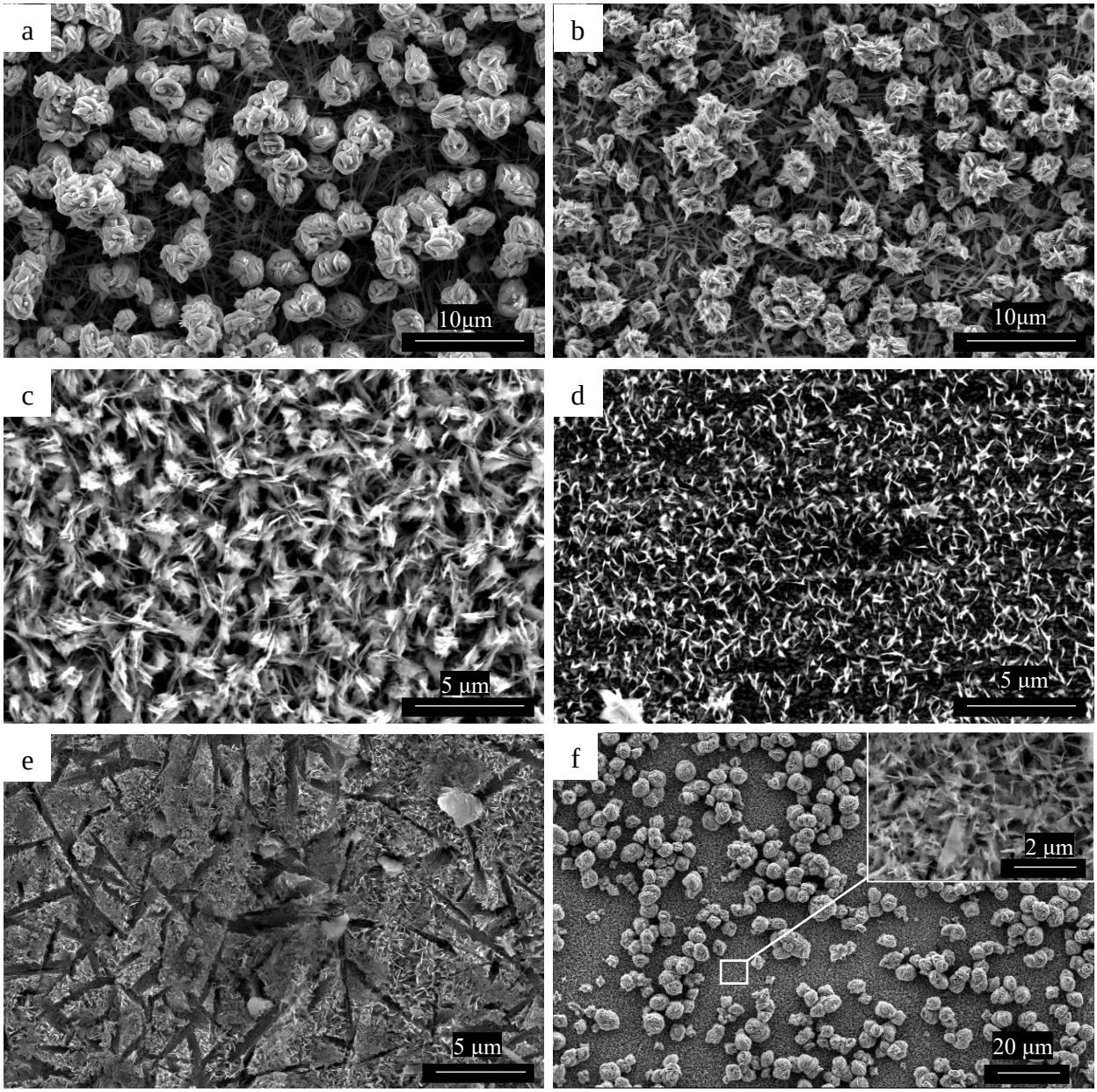

Figure 2.6 Representative SEM images of the various nanostructures obtained via full-factorial experiments (a) round nanoflowers (RNF) and nanograsses (NG), (b) spiky nanoflowers (SNF) and nanograsses (NG), (c) long nanoneedles (LNN), (d) short nanoneedles (SNN), (e) nanotrenches (NT), and (f) round nanoflowers on nanomesh (NM).

The abbreviations of the nanostructures with their respective characteristic lengths are presented at the bottom row in table 2.2. In addition, figure 2.6a-f shows the SEM images of all possible nanostructures obtained using the parameter variations mentioned in table 2.2. Table 2.2 also shows the characteristic lengths of all the nanostructures measured using ImageJ. Interestingly, the two-level nanostructures consist of a top layer of nanoflowers (NF~3-4 μm) resting on a layer of nanograsses (NG~3-4 μm). Such nanoflowers and nanograsses are only observed at lower solution temperatures (< 40^{o}C) for all solution concentrations (B1, B2, and B3) and immersion time (3mins to 60 mins). Furthermore, solutions B1 and B3 with different NaOH content produce two-level nanostructures with two different nanoflower morphologies – round nanoflowers (RNF) (figure 2.6a) and spiky nanoflowers (SNF) (figure 2.6b). With an increase in solution temperature (>40^{o}C), the unstable nanoflowers and nanograsses dissolve in the solution exposing a bed of nanoneedles with two sizes - long nanoneedles (LNN~2 μm) (figure 2.6c) and short nanoneedles (SNN~0.3 μm) (figure 2.6d). The length of nanoneedles is decided by the solution composition, a mechanism for which is unclear. In addition, as the nanograsses dissolve, they also leave behind nanotrenches (NT~3-4 μm) (figure 2.6e) as imprints. Finally, solution B2, with an intermediate basicity, yields a nanomesh (NM) structure studded with round nanoflowers (figure 2.6f).

It is convenient to fabricate and control the number, size, and shape of the two-level nanostructures, *i.e.* nanoflowers/nanograsses by controlling the solution composition and immersion time. Consequently, we select solutions B1 and B3 to study the morphological impacts of round and spiky nanoflowers by varying the immersion time from 1 min to 25 mins on the CAs.

2.3.2 Morphological Analysis of Nanoflowers and Nanograsses

The combination of chemical solutions of NaOH and $K_2S_2O_8$ (*i.e.* B1 and B3) creates heterogeneous surfaces possessing two-level features such as nanograsses and nanoflowers. In the

oxidation process of those surfaces, nanograsses and nanoflowers exhibit different nucleation density and rate, creating time-dependent nanostructure morphologies that can be categorized by grass- and flower-dominated regime.

In detail, nanograsses initially start growing on the substrate within the 'grass-dominated regime' until $t = t_c$, the critical time, where the transition between morphological regimes occurs at flower area ratio $f_{NF} = 0.5$. After $t > t_c$, the nanoflowers keep increasing their sizes with immersion time by the Ostwald ripening mechanism[37], and occasionally agglomerate to form short chains and piles, in the 'flower-dominated regime'.

The different chemical compositions in the oxidation process affect the morphology of nanograsses and nanoflowers due to their level of alkalinity in the solutions[38]. Solution B1 produces round-shaped nanoflowers and thin, long nanowires, defined as 'round nanoflower' and

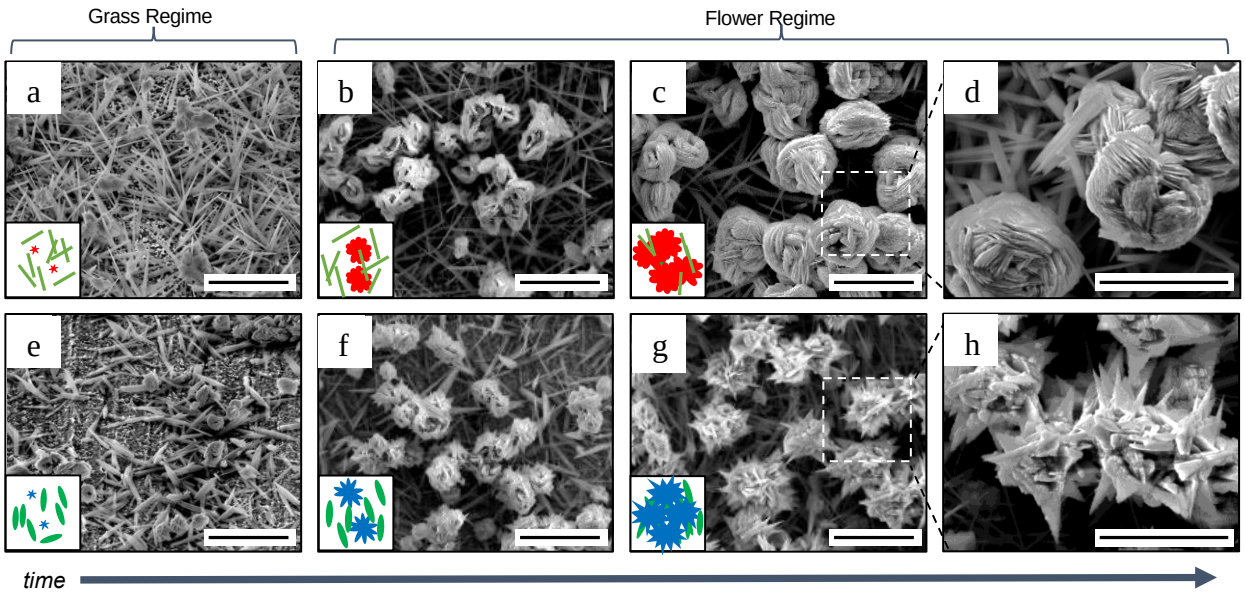

Figure 2.7 Scanning electron microscope (SEM) images of time-evolving nanostructures using different combination of chemical solutions. Round nanograsses and nanoflowers are prepared at immersion time (solution B1) of (a) t = 3, (b) 10, and (c-d) 15 mins. Using different chemical concentration, spiky nanograsses and nanoflowers (solution B3) at (e) t = 3, (f) 10, and (g-h)15 mins are observed. The close-up views of (d) and (h) show round- and spiky-shaped flower petals, respectively. Insets illustrate the evolution of nanograsses and nanoflowers with immersion time. All scale bars are 5 μm.

'round nanograss', as indicated in the scanning electron microscope (SEM) images in figure 2.7a-d and figure 2.8i. The lower NaOH concentration in solution B3 yields spike-shaped features and wide, short nanowires, defined as 'spiky nanoflower' and 'spiky nanograss' (SEM images in figure 2.7e-h and analysis in figure 2.8i). The preferential growth of nanograsses occurs at surface defects (*i.e.* impurities, scratches, grain boundaries) that determine the number of nanograsses, quickly leading to saturation. The tightly-packed nanograsses on such limited spaces of surface defects are prone to depart from the surface and begin to agglomerate, forming cluster-like nanoflowers in order to reduce their surface energy[39]. The differences in the nanoflowers' petal shapes are expected to be contributed by the amount of nanograss agglomeration that occurs. That is, a highly basic solution (solution B1) causes a more active nanograss agglomeration, rounding the nanofeatures to produce round nanoflowers. Whereas low agglomeration level of spiky nanograsses causes rough-edged petals to form.

The image quantification of nanofeatures is conducted by investigating both top and side view SEM images (figure 2.8a and b). The top view SEM images are used to quantify the morphological details of nanograsses and nanoflowers (*i.e.* the area ratio ϕ, diameter d, number density n, length l, and width w) where the subscripts NG and NF denote the nanograss and nanoflower, respectively. The side view images are obtained using focus ion beam (FIB) technique that mills the structure to enable a top-angled view. The side view images through the FIB SEM technique allow us to calculate nanoflower heights h_{NF} and maximum peak height $h_{NF,max.}$ Based on those top and side view 2D images, 3D topographical images can be reconstructed to compute the roughness r by using a commercial software (MountainsMap) with the ISO 25178 standard[40]. This post-image processing analyzes the difference in contrast and brightness of an image of interest to

construct a relative topographical map with the estimation of $h_{NF,max}$. As a result, a representative 3D topography image of round nanoflowers is shown in figure 2.8c.

The plot in figure 2.8h showing nanoflowers area ratio ϕ_{NF} confirms the nanofeature growth can be classified into two distinguishable regimes: nanograsses-dominated ($t < t_c$) and nanoflowers-dominated ($t > t_c$) regimes, where ϕ_{NF} is the ratio of the sum of individual flower area to the total area. The transition between two-level morphologies occurs due to the different growth rates of nanograss and nanoflowers and are shown to approximately occur at t_c = 7 mins in this study. In addition to the area fraction calculation, the nanoflowers' diameter d_{NF} and maximum height $h_{NF,max}$ with varying immersion time are plotted in figure 2.8d and e. The d_{NF} and $h_{NF,max}$ is directly measured from 2D SEM images from top and side view. Over the entire time, the round nanoflowers' diameter is consistently 10-30% larger than that of spiky nanoflowers. Larger diameters of round nanoflowers result in smaller number density than that of spiky nanoflowers once the regime is stabilized at $t > t_l$ = 15 mins (figure 2.8f). At this saturation time, both d_{NF} and $h_{NF,max}$ remain constant at 3-4 μm and 5-7 μm, respectively while the ϕ_{NF} continue to increase up to ~0.6 (figure 2.8h).

Another important structural parameter that affects the wettability of nanostructured surfaces is the roughness *r*, defined as the ratio of interfacial surface to projected surface, thus a flat surface will possess *r*=1. The *r* values with varying morphology are computed using 3D images (shown in figure 2.8g). The *r* of round nanostructure is 75% larger than that of spiky nanostructure in the grass-dominated regime ($t < t_c$) due to its larger nucleation density. In the flower-dominated regime ($t>t_c$), the *r* of round nanoflowers is 25-50% smaller than that of spiky nanoflowers. Such a noticeable increase in the *r* of spiky nanoflowers is contributed by the spiky nanoflowers' sharp-edged petals as well as larger *n* in the flower-dominated regime.

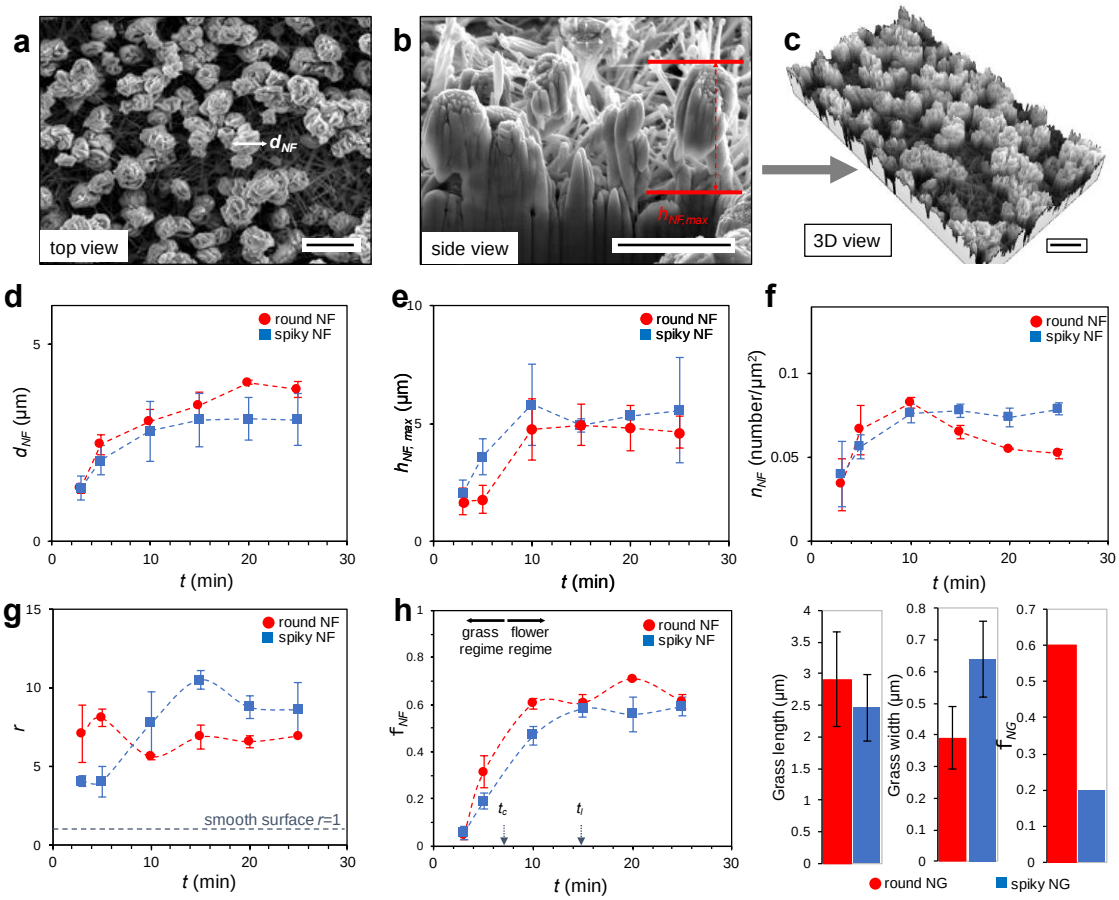

Figure 2.8 Effects of chemical immersion time on nanostructure morphologies. Representative SEM images of round nanostructures from (a) top and (b) side-angled view at t = 15 mins. (c) The top and side views enable the reconstruction of the three-dimensional topography to calculate the roughness of the nanostructures. Image analysis is followed to investigate the morphological details of nanoflowers including (d) nanoflowers' diameters d_{NF}, (e) maximum height h_{NF}, (f) number density n_{NF}, (g) roughness r, and (h) the area ratio ϕ_{NF}. (i) The structural information including length l_{NG} and width w_{NG} of nanograss features is plotted. (Scale Bar=5 μm)

In detail, 2D SEM images and a maximum height of the structure are plugged in as inputs to the software. This image processing analyses the difference in contrast and brightness of an image to construct a relative topographical map of the image. The value of maximum peak height is estimated based on Focus Ion Beam (FEI Quanta 3D FEG Dual Beam) SEM images as plotted in figure 2.8e.

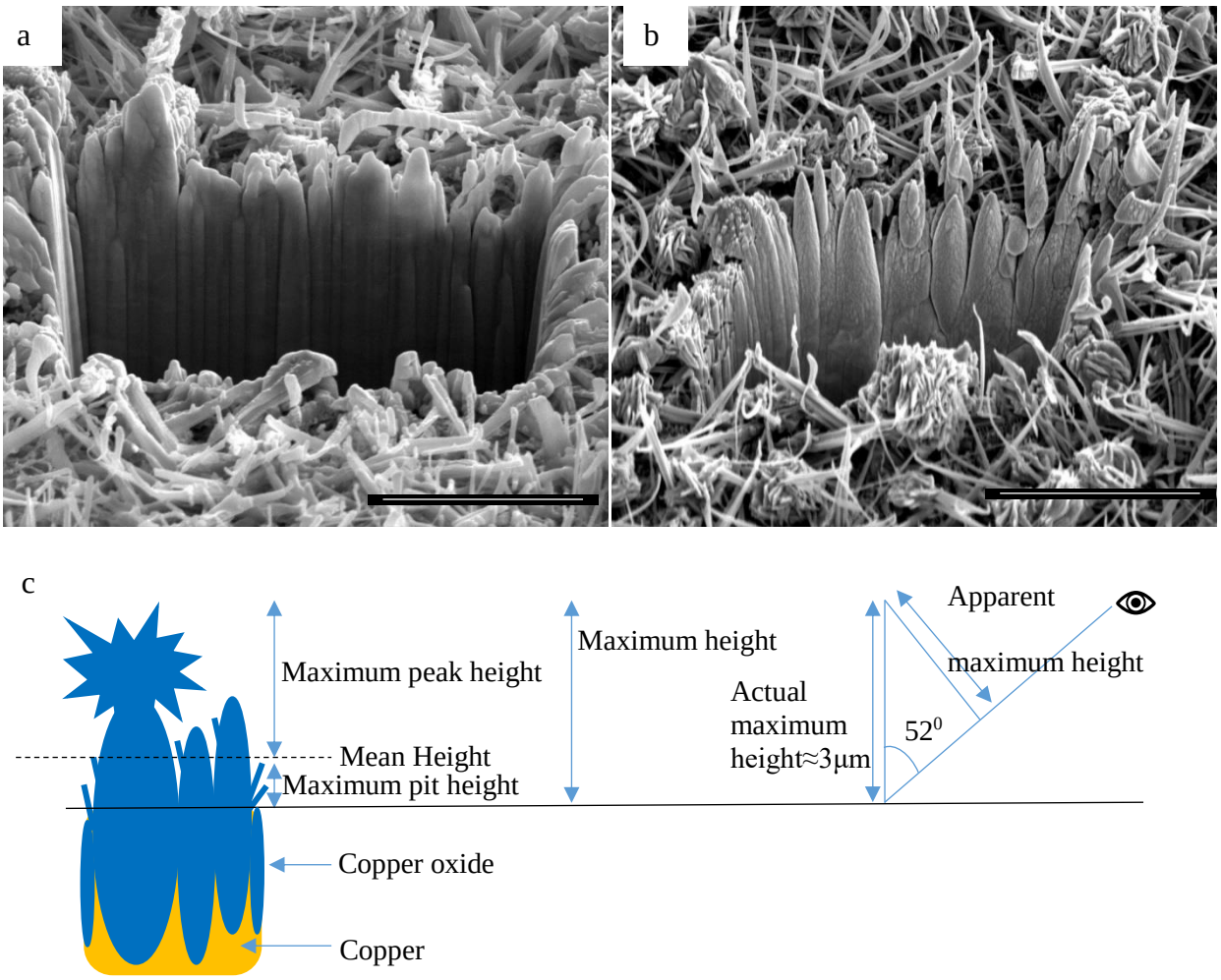

Figure 2.9 FIB-SEM images of round (a) and spiked (b) NFs fabricated a 15 mins' immersion used to feed 'maximum height data' to 3D reconstruction software (scale bar is 5µm), and (c) parameters defined for roughness calculations using MountainsMap®.

The cross-sectional images in figure 2.9a,b clearly confirm the dendritic growth of nanoflowers. Round NFs with a processing time of 15 mins (figure 2.9a) show a comparatively smoother surface with thicker and rounder nanograsses fabricated comparing with spiky NFs. The apparent maximum height is calculated from the lowest point to the highest point on the milled surface (figure 2.9c) based on the angle between electron and ion columns of 52°. So the actual

maximum height is found to be approximately 3 µm. As a result, figure 2.8a,c shows the examples of 2D SEM and 3D reconstructed image of round nanoflowers. Based on 3D topography, the height of the nanostructures is computed as a function of a traced line length as shown in figure 2.10c.

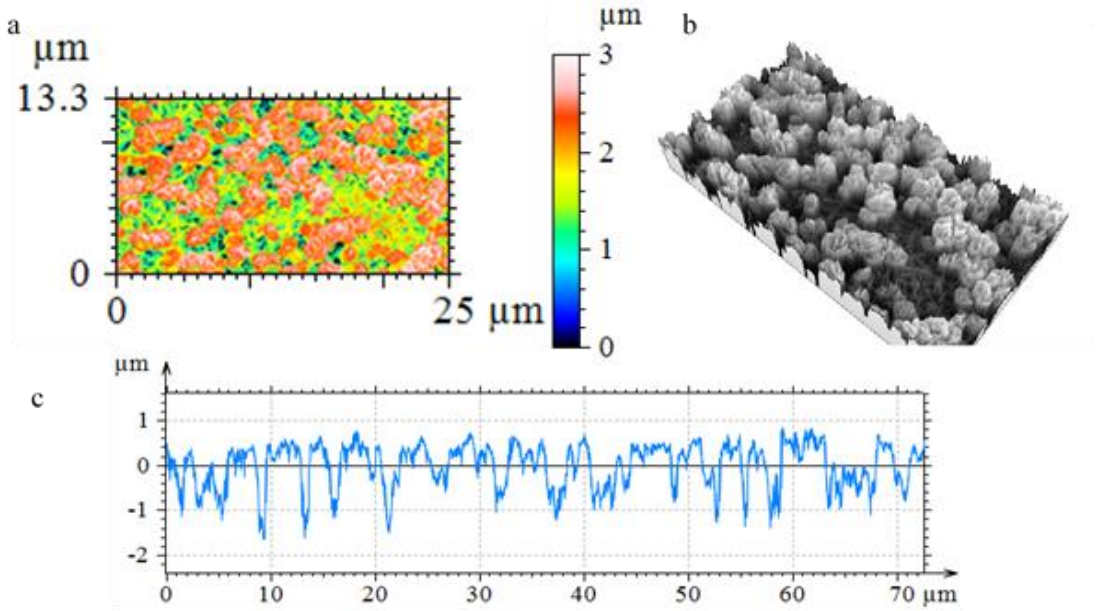

Figure 2.10 3D reconstruction of a single SEM image of round nanoflowers fabricated at 15 mins' immersion, (a) topological plot, (b) 3D visualization, and (c) roughness profile recorded with a zig-zag trace on the SEM image.

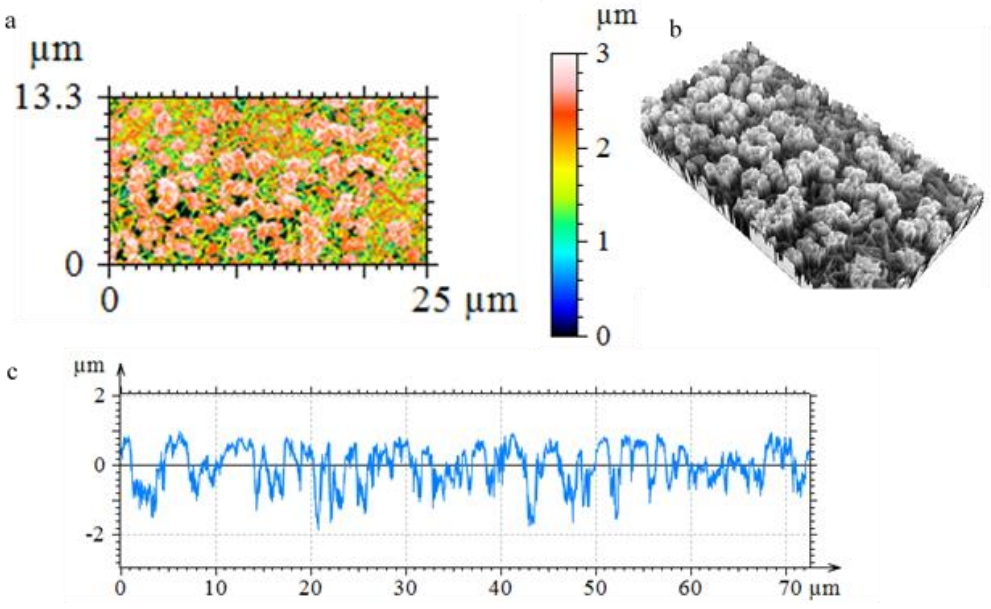

Figure 2.11 3D reconstruction of a single SEM image of spiky nanoflowers fabricated at 15 mins immersion, (a) topological plot, (b) 3D visualization, and (c) height profile recorded with a zig-zag trace on the SEM image.

Table 2.3 Parameters evaluated from the 3D reconstructed images at 15 mins immersion

Parameters	Round nanoflower	Spiky nanoflower
Root-mean-square height (Sq)	0.682 µm	0.832 µm
Maximum peak height (Sp)	1.07 µm	1.09 µm
Maximum pit height (Sv)	1.93 µm	1.91 µm
Skewness (Ssk)	-0.978	-1.04
Kurtosis (Sku)	3.66	3.29
Arithmetic mean height (Sa)	0.551 µm	0.656 µm
Developed interfacial area ratio (Sdr)	625 %	985 %

Representative results of the 3D reconstruction using round (figure 2.10) and spiky (figure 2.11) nanoflowers fabricated at 15 mins' immersion show the (a) topological plots, (b) 3D images, and (c) height vs zig-zag trace profiles. Such data processing is repeated for several images at each immersion time and the developed interfacial area ratio (Sdr) is evaluated from the height profile. Furthermore, table 2.3 lists the average of the roughness parameters evaluated using the ISO 25178 standard. The skewness and kurtosis for both nanoflowers are approximately the same, proving the distribution is equally skewed. This is noted as a quantitative indicator that the images are collected at equal contrast and brightness values for a fair comparison. Notice that the roughness factor (r) is the ratio of actual surface area to projected surface area whereas the developed interfacial area (Sdr) is the ratio of liquid-solid interfacial area to projected surface area. Thus, the correlation between r and Sdr is expressed as $Sdr = 100(r\text{-}1)$ (%). With the fabricated structures, round nanograsses show larger roughness than spiky nanograsses in a grass-dominated regime while spiky nanoflowers show larger roughness in a flower-dominated regime.

The method of 3D reconstruction enables fast generation of 3D topography with a moderate accuracy and low costs compared to Atomic Force Microscopy (AFM) analysis while AFM is limited because of the costs and errors from the 'tip convolution' effect[41]. To improve the accuracy of 3D topographies, SEM images should be carefully recorded with maximum contrast without losing the depth of focus. Fast height measurement is possible by FIB-SEM imaging, which enables better visualization (without obstruction from nanograsses) in a short time with minimal sample invasion.

2.3.3 Surface Chemical Composition Analysis

We perform the point-by-point energy dispersive spectroscopy (EDS) analysis to understand how the chemical composition of individual nanofeature affects their wetting properties. The ratio of surface Cu:O content for both round and spiky nanofeatures is plotted as a function of immersion time in figure 2.11a and b. In figure 2.12a, round nanograsses in the grass-dominated regime show a larger ratio of surface Cu:O=0.3-0.4 ($t < t_c$) than round nanoflowers (Cu:O=0.1-0.2) where the surface is mostly covered by grasses (instead of flower). Thereby, the resulting wetting properties

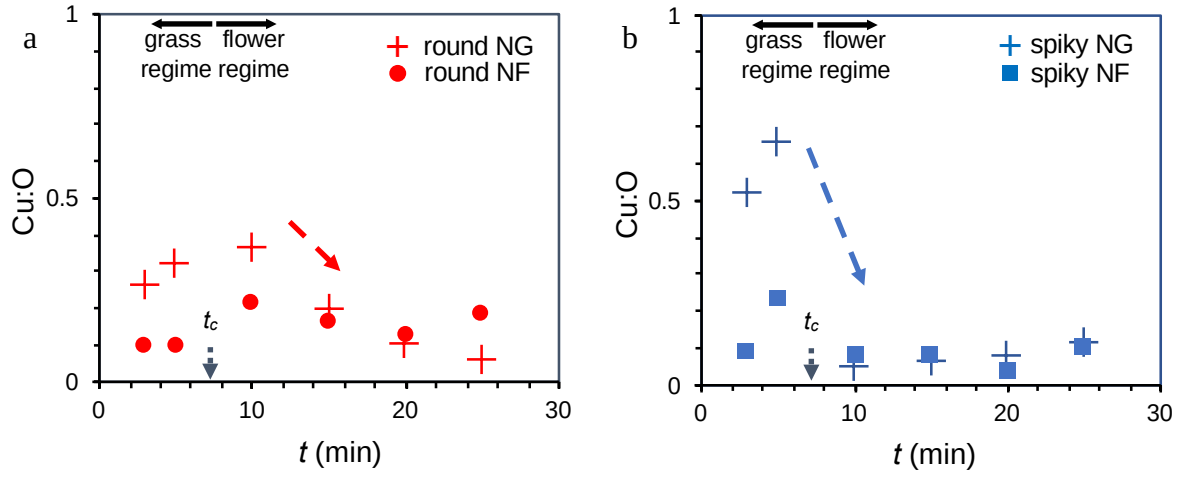

Figure 2.12 Nanostructure chemistry changes using energy dispersive spectroscopy (EDS) analysis. The ratio of surface copper to oxygen is presented for (a) round and (b) spiky nanofeatures with varying immersion time. The highlighted regime indicates a higher copper content in nanograsses at $t < t_c$.

of round nanostructures ($t < t_c$) will be determined by the greater presence of copper as indicated in figure 2.15a. In figure 2.12b, spiky nanograsses in the grass-dominated regime show a much larger ratio of surface Cu:O=0.6 ($t < t_c$) while spiky nanoflowers show a lower ratio of surface Cu:O=0.1-0.2. However, the nucleation density of spiky nanograss is smaller than that of round nanograss. The resulting nanograss area ratio ϕ_{NG} =~ 20% (figure 2.9i) at t = 3 mins minimizes the impact of copper-containing spiky nanograsses on the wetting properties, as indicated in figure 2.15a. As time evolves in the flower-dominated regime, the ratio of surface Cu:O content of all four entities gradually reduces (*i.e.* the level of oxide increases) to generate hydrophilic surfaces. Based on the morphologies and chemistry of nanofeatures, the phase diagram in figure 2.15a shows the governing surface chemistry (copper vs. oxide) depending on the structural evolving stages (grass-dominated regime vs. flower-dominated regime) for both morphologies (round and spiky features). In this phase diagram, round and spiky nanograsses ($t < t_c$) possessing more copper suggest relative hydrophobicity while nanoflowers show more oxide components.

The nanostructure surface chemistry is investigated using Relative Intensity Ratio (RIR) of Grazing Incidence X-ray Diffraction (GI-XRD) patterns (GI-XRD, *Rigaku Smartlab X-Ray Diffractometer*)[42]. The GI-XRD pattern shows that both round and spiky nanoflowers are composed of CuO and $Cu(OH)_2$ where the intensities increase with chemical immersion time (figure 2.13). In general, the intensity of both CuO and $Cu(OH)_2$ increases (circle a) while Cu decreases (circle b) with increasing immersion time. Relative-Intensity-Ratio (RIR) method for GIXRD obtains surface phase weight percentage (figure 2.14) clearly shows a drastic increase in weight percent of CuO with a simultaneous decrease in weight percent of Cu with immersion time. The increase in the surface $Cu(OH)_2$ content is relatively small compared to that of CuO. This is

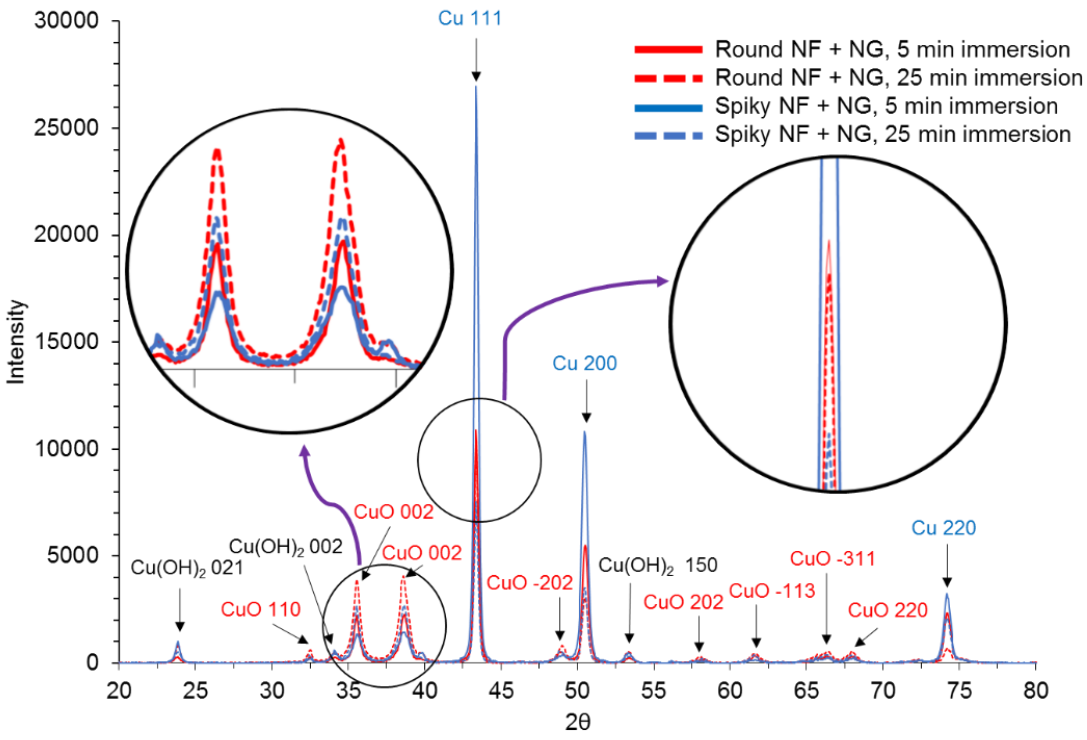

Figure 2.13 GI-XRD pattern of round and spiky nanoflowers at 5 mins' and 25 mins' immersion.

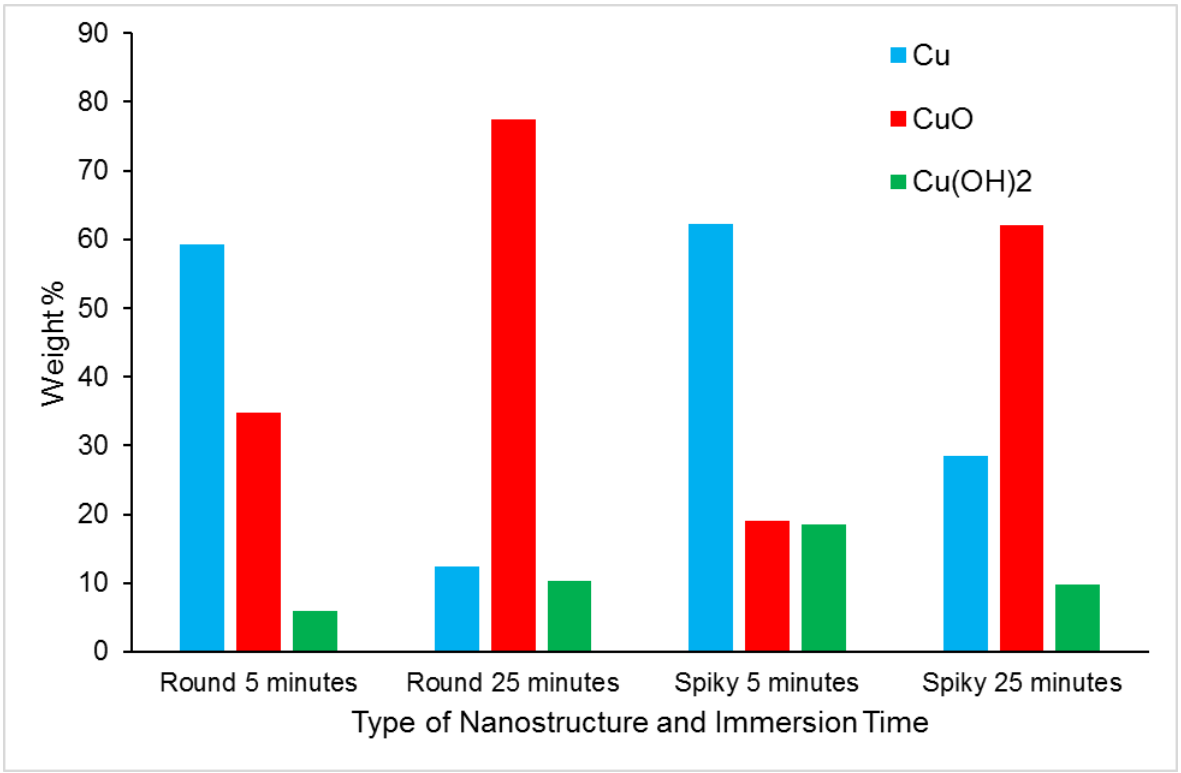

Figure 2.14 Surface weight percentage of round and spiky nanoflowers immersed for 5 mins and 25 mins.

because $Cu(OH)_2$ is relatively metastable and the formation of CuO nanoflowers is accompanied

by the breaking of H-bonds at the edges of $Cu(OH)_2$ layers[35,43].

This analysis also observes that spiky nanoflowers show higher weight percent of Cu on the surface than round nanoflowers. This might be attributed to a lower concentration of NaOH used during solution oxidation. At lower immersion time, the weight percent of CuO and $Cu(OH)_2$ is approximately equal. However, at t = 25 mins, Cu and $Cu(OH)_2$ transform to CuO indicating the formation of nanoflowers originating from nanograsses.

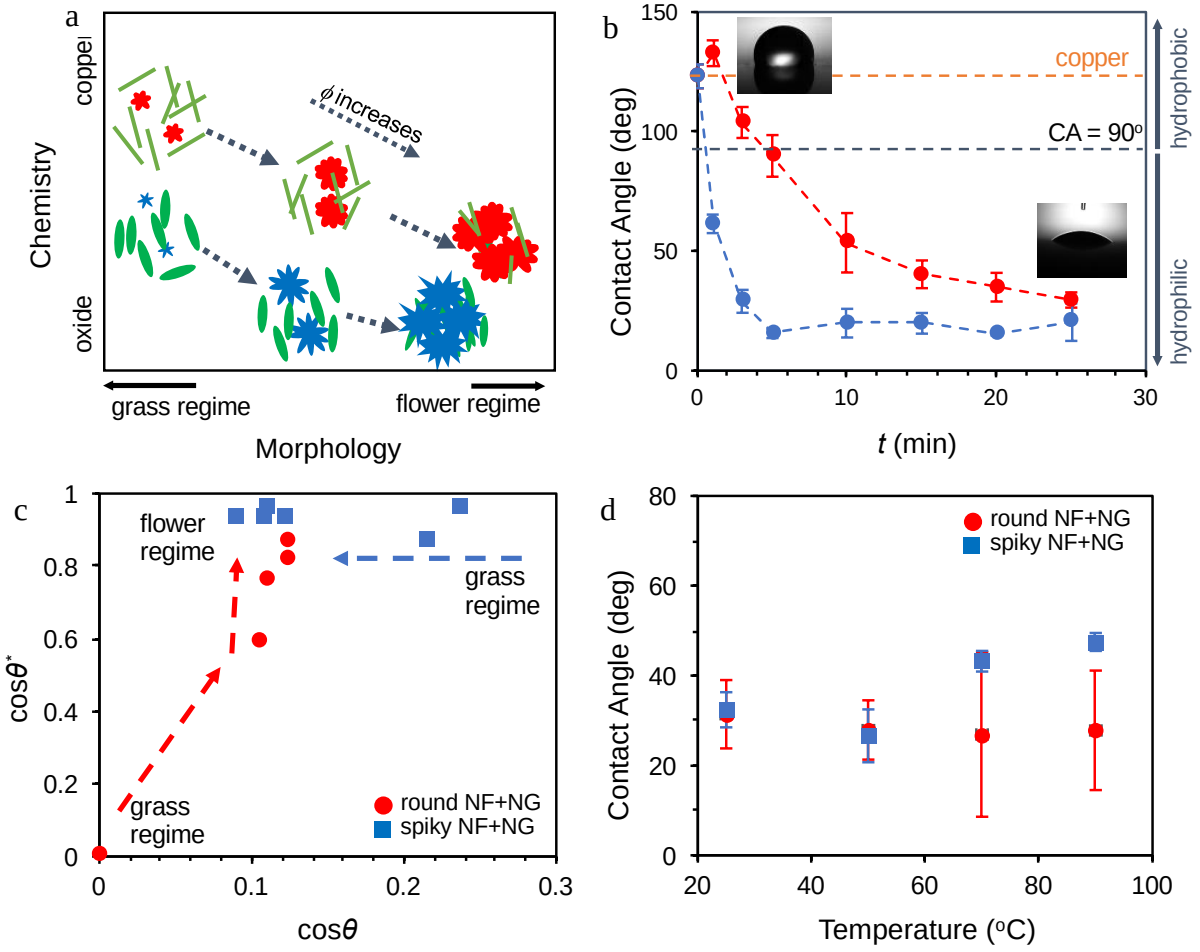

Figure 2.15. (a) Phase diagram showing the dependency of surface chemistry (copper regime vs. oxide regime) on morphology (grass-dominated regime vs. flower-dominated regime) as examined with EDS analysis. (b) Wettability measured for both round and spiky nanofeatures with varying immersion time shows decreasing CAs *with immersion time. (c) Variation in* $\cos\theta^*$ *with* $\cos\theta$ *for round and spiky nanostructures demonstrates that surface roughness governs the wetting behaviors in flower-dominated regime while surface chemistry dominates the grass-dominated regime. (d) Temperature-dependent* CAs *for round and spiky nanostructures (t =25 mins).*

2.3.4 Wetting Characteristics

After observing the changes in surface morphologies and chemistries, we evaluate the wetting characteristics of the fabricated surfaces by measuring their CAs. For this, we use a contact angle meter (MCA-3, Kyowa Interface Science) that dispenses nanoliter-sized droplets. A high-speed camera at 100,000 fps captures transient and temperature-dependent liquid-vapor interfaces on structured surfaces. The contact angle measurements are recorded at 10 different locations on each sample. The results in figure 2.15b show the measured CAs as a function of immersion times. In the grass-dominated regime, round nanograsses exhibit relatively hydrophobic wettability, showing the CAs of 110-70^{o}. This might be attributed to the dominance of surface copper in nanograsses as illustrated by the phase diagram in figure 2.15a. Since the regimes are predominantly covered by nanoflowers as *t* increases, both round and spiky nanoflowers contain more surface oxide, showing hydrophilicity. Spiky nanoflowers consistently show low CAs as an evidence of hydrophilicity because of the combination of surface chemistry and sharp morphology.

The role of structural information and chemistry related to surface wettability can be explained by Wenzel's[15] or Cassie's model[16]. In Wenzel's model, a liquid is assumed to completely fill the grooves of a rough surface while vapor pockets are assumed to be trapped underneath a liquid drop, creating a composite surface in Cassie's model. Since most surfaces reported in this study are hydrophilic, we employ the Wenzel's analysis to explain the relationship between surface chemistry and its wettability. In this analysis, θ (~75-90^{o}) is calculated using θ^{*} (CAs on nanostructured surfaces) and *r* from image analysis based on the Wenzel's equation 1.2. The data sets are placed in the Wenzel quadrant, as plotted in figure 2.15c. Both round and spiky nanofeatures show a relatively noticeable difference $d\theta$ (~15^{o}) between the regimes, confirming the differences in structural chemistry from grasses to flowers. Again, both round and spiky

nanostructures show a small deviation $d\theta$ (~5°) at $t > t_c$, revealing that r governs the wettability. The use of Wenzel's equation is valid in this study because the droplet diameter (300-400 μm) is two orders of magnitude larger than the characteristic length of the nanostructures (~5-8 μm)[17,18] while the gravity effect is negligible.

In addition to the modulation of CAs via tuning the nanoscale growth morphology, it is important to investigate the temperature-dependent wetting properties of such nanofeatures our most hydrophilic samples (*i.e.* fabricated at t = 25 mins) for the use in heat pipe applications because of their potential use in heat transfer devices. In particular, it is of interest to investigate our most hydrophilic samples (*i.e.* fabricated at t = 25 mins) for the use in heat pipe applications at elevated temperature[1,11]. Here, we vary the substrate temperatures ranging from 25°C to 90°C using a thermal stage attached to the substrate to measure the temperature-dependent CAs as

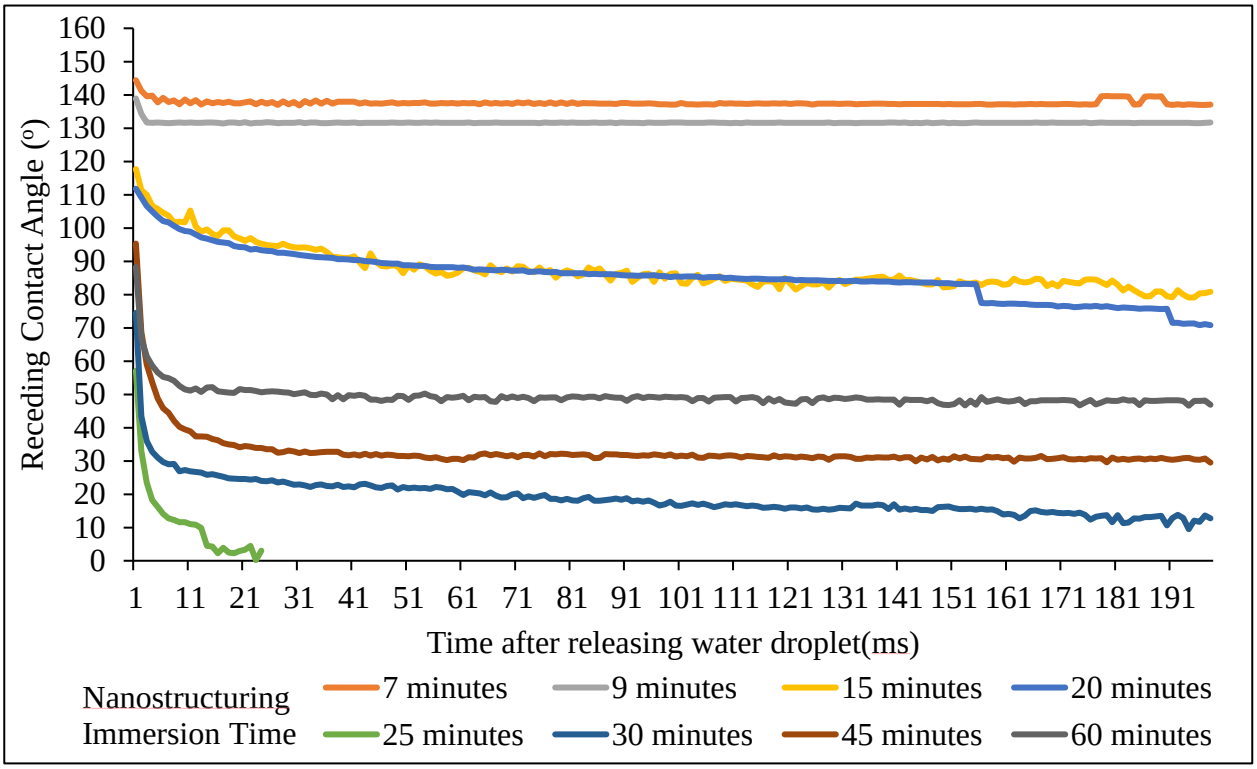

Figure 2.16 Receding contact angle vs time after releasing the water drop for nanostructured copper surface.

plotted in figure 2.15d. In this process, temperatures are confirmed with a thermocouple taped to the thermoelectric modules and the sample surface. Spiky nanoflowers show a gradual increase in CAs with increasing temperatures whereas round nanoflowers show constant CAs. This phenomenon might be attributed to the formation of local vapor blankets below the highly rough spiky nanoflowers. In general, this measurement confirms that nanostructures with low CAs are consistent at high temperatures.

Additionally we examine the change in receding CAs with immersion time (figure 2.16). The receding CAs decrease with an increase in immersion time and reach the superhydrophilic limit at 25 mins of immersion. Furthermore the receding CAs are $< 90^{o}$ only when $t \geq 25$ mins suggesting 25 mins is the minimum immersion time to achieve hydrophilic characteristics.

In this chapter, we have investigated the effects of fabrication parameters of solution immersion methods to determine nanostructures' morphological details and their chemistry. First of all, by using two different sets of chemical solution A or B, we fabricate different nanostructure shapes such as nanoflakes or nanograsses and nanoflowers, respectively. Consequently, the CAs of copper oxide nanostructures are measured and are related with their structural information and chemical composition.

CHAPTER 3: DEMONSTRATION OF HIERARCHICAL STRUCTURES

Porous copper structures with nanostructures can be utilized for microfluidic wicking applications[44], antibiofouling[4], anti-icing[45], and efficient condensation heat transfer[25] applications. The design of the hierarchical copper nanostructures combining two different length scales can improve wicking applications by providing an enormous fluid-permeable accessibility. In those applications, it is critical to maximize solid-liquid interfacing surface areas with desired hydrophilic properties to improve fluid transport within void fraction of porous structures. Therefore, in Chapter 3, we study how to fabricate hierarchical copper structures by employing microporous copper structures and solution immersion methods that are discussed in Chapter 2.

3.1 Copper Inverse Opals

The heat flux through porous copper structures in thermal wicks, which is explained by the modified Darcy's law[46], is proportional to permeability K and is inversely proportional to effective pore diameter D_{eff}. From the Darcy correlation, a higher permeability requires larger pore sizes in order to minimize the viscous resistance through porous structures. Also, a higher permeability can be obtained by both small pore sizes D_{eff} and small CAs θ where the effective pore diameter $D_{eff} = D_{pore}\cos\theta^{-1}$.

Among multiple types of porous copper structures such as sintered copper particles[47] or machined copper structures[48], copper inverse opals (IO)[49] are shown to be appealing because of their periodicity, regularity, and pore-level controllability. The unique combination of such structural characteristics enables the control of geometrical designs including porous copper's porosity and tortuosity. The control will enable to precisely control thermal and liquid transport through the solid and void fractions of porous copper. Therefore, copper IOs are selected for the creation of hierarchical porous copper with nanostructure installation with the aim of maximizing

their interfacial surface area. SEM image of copper IOs (figure 3.1) shows a side view of the pores and necks that provide a tortuous path for the fluid to flow.

3.2 Fabrication of Hierarchical Copper Inverse Opals

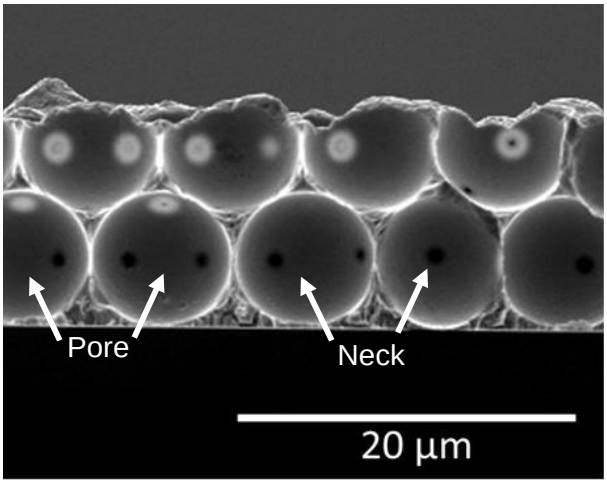

Figure 3.1 SEM image of copper inverse opals showing the interconnected pores of 5 µm in diameter.

Hierarchical copper IOs are fabricated by combining a template assisted electrodeposition technique around self-assembled monodispersed spheres and solution immersion methods that are discussed in Chapter 2. A schematic of the complete fabrication process can be found in the previous research[51] and is briefly illustrated in figure 3.2a-d. The general fabrication process is briefly explained below:

- Polystyrene spheres of diameter ~ 8 µm are deposited on a gold substrate using either vertical deposition process or drop casting process and sintered at elevated temperature (~98 ^{o}C).
- These spheres self-assemble to form close packed structures, are dried at room temperature, and are annealed at ~100^{o}C. The self-assembly is driven by the attractive capillary force interaction which reduces the Gibbs free energy. A combination of hydrodynamic forces

and capillary forces is responsible for dragging and trapping the spheres within a thin liquid film[50] (figure 3.2a).

- The electrodeposition of copper around the sacrificial polystyrene spheres using a potentiostat will be followed (figure 3.2b).
- The polystyrene spheres are dissolved using tetrahydrofuran to leave behind hollow copper structures, known as copper inverse opals (figure 3.2c).
- Finally, we perform the solution immersion process to fabricate nanostructures on copper inverse opals (figure 3.2d).

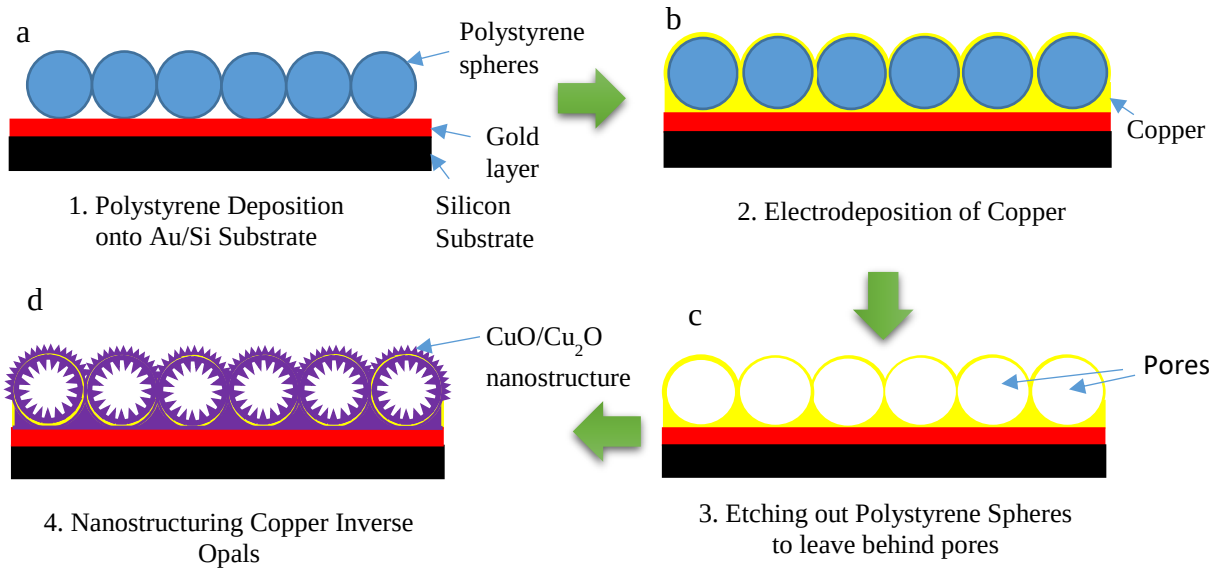

Figure 3.2 (a) Self-assembly of polystyrene spheres, (b) electrodeposition of copper around polystyrene spheres, (c) removal of polystyrene spheres, and (d) nanostructure installation on copper inverse opals (IOs).

3.3 Hierarchical Copper IOs with Nanoflowers/Nanograsses (Solution B1)

Copper IOs are hydrophobic showing a CA of 140^{o} without any surface treatments. Taking a cue from the nanostructure process using bare copper substrates, the solution immersion method can install superhydrophilic nanoflowers/nanograsses on copper IOs. In this process, 5 μm sized copper IOs are immersed in solution B1 for an immersion time ranging from 3 mins to 60 mins at room temperature (figure 3.3a-f).

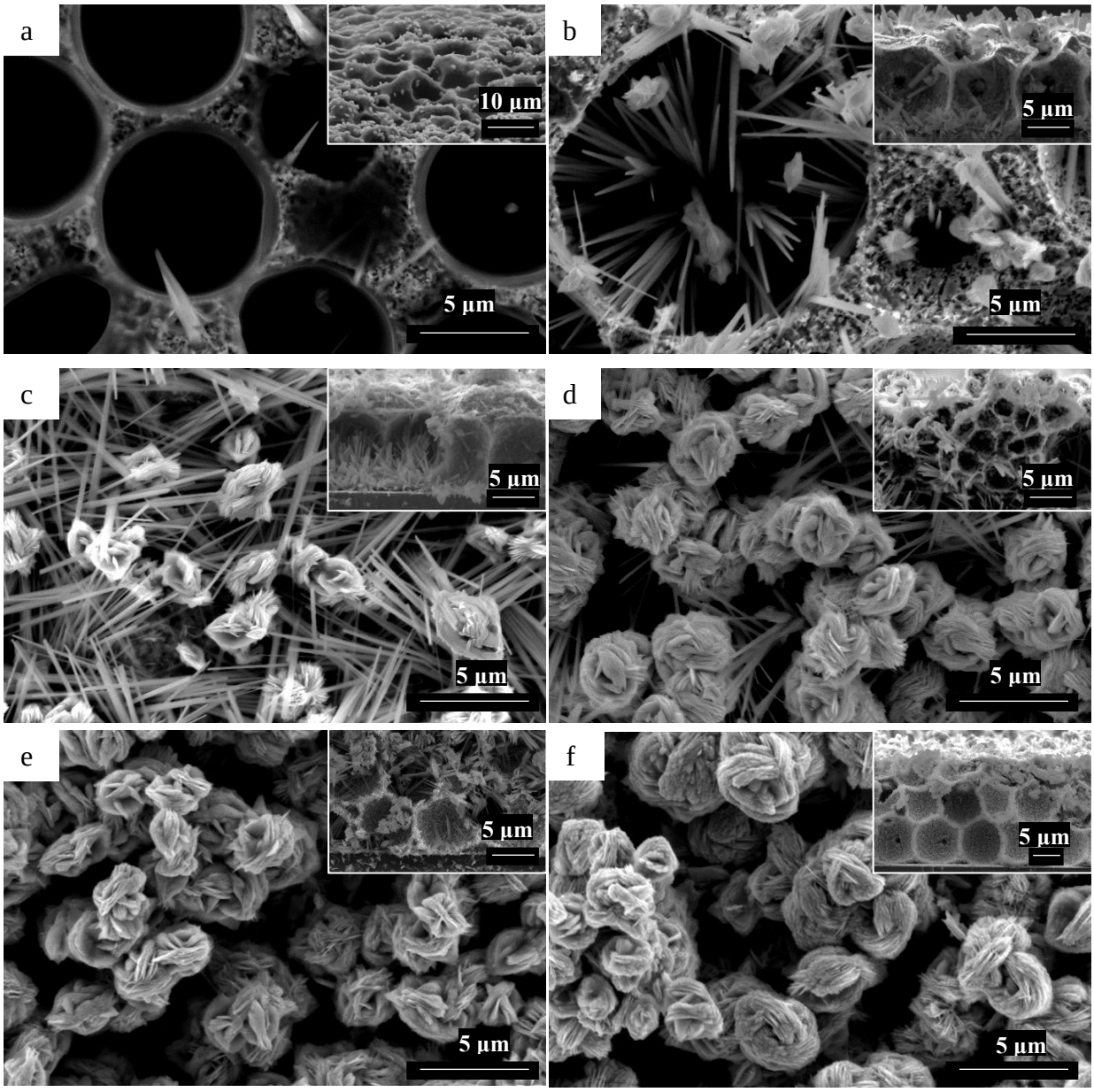

Figure 3.3 SEM images of copper inverse opals decorated with nanoflowers with solution B1 (insets show side view) at immersion time of (a) 3 mins, (b) 5 mins, (c) 10 mins, (d) 15 mins, (e) 30 mins, and (f) 60 mins.

3.4 Wetting Characteristics of Nanostructured Copper IOs

The static CAs of the nanostructured copper IOs are measured using the contact angle meter. As observed in figure 3.4, the CAs gradually reduce with increasing immersion time, which shows a similar trend of the bare coppers' wetting characteristics (from Chapter 2). The plot in figure 3.4 shows superhydrophilicity when immersion time ≥30 mins.

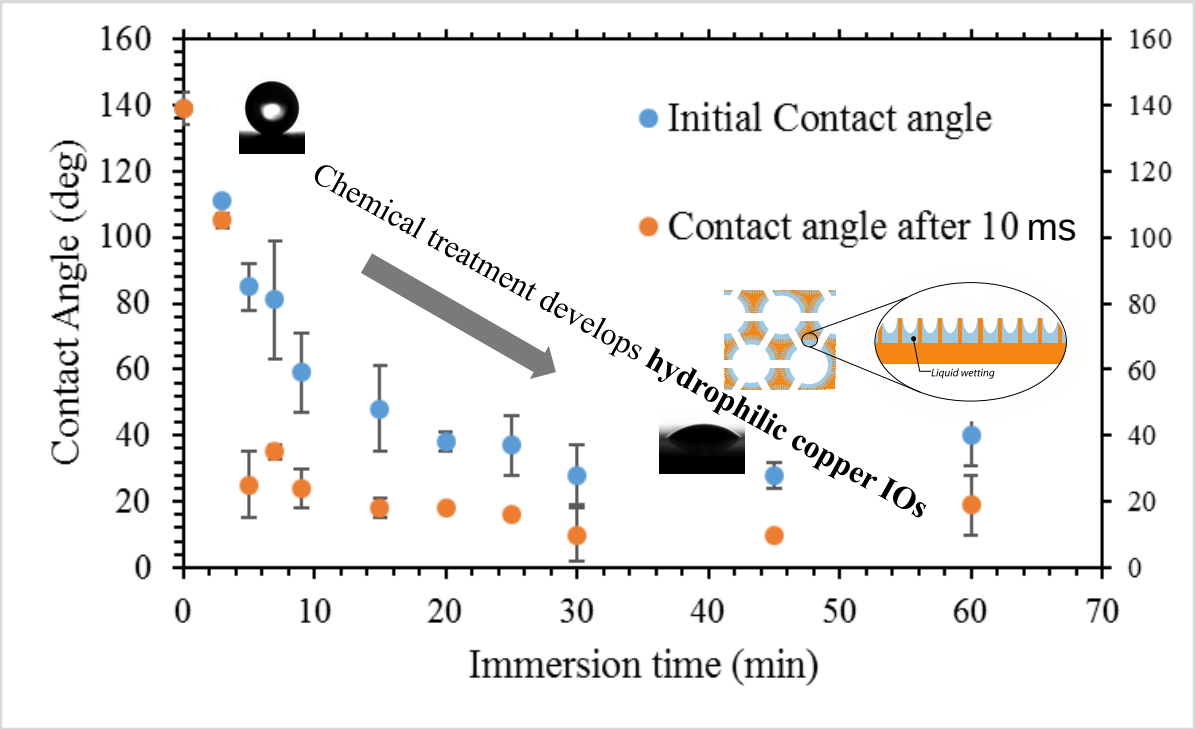

Figure 3.4 Contact angle vs immersion time for nanostructured copper IOs shows superhydrophilicity for 30 mins or higher immersion time.

Additionally, we compare the receding CAs for nanostructured copper IOs with that for nanostructured polished copper substrates. As observed in figures 3.5 and 2.16, the receding CAs for nanostructured copper IOs are hydrophilic at t > 5 mins whereas nanostructured polished copper substrates are hydrophilic at t > 25 mins. These observations suggest us that:

- The CAs on hierarchical copper inverse opals are inversely proportional to the immersion time, and hydrophilicity is achieved within 5 mins of immersion.

- The optimum immersion time for superhydrophilicity on nanostructured copper plates and nanostructured copper IOs is approximately 25 mins where the CAs remain constant.

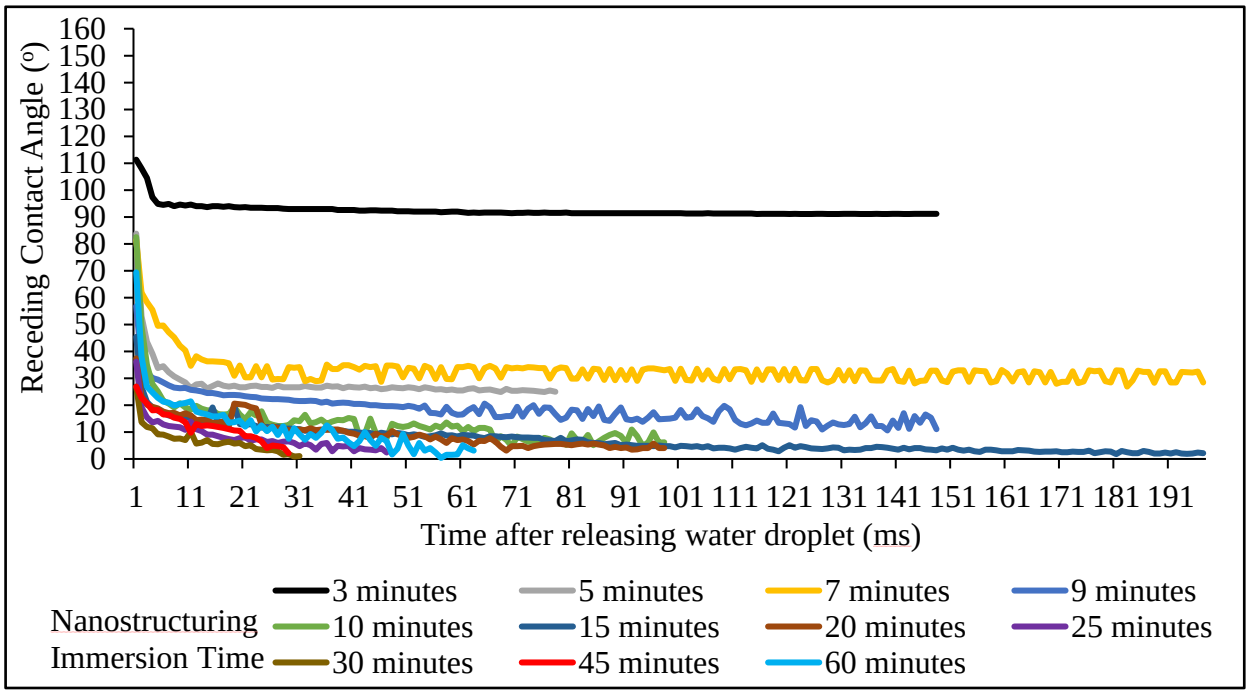

Figure 3.5 Receding contact angle vs time after releasing a water droplet on nanostructured copper IOs.

The nanostructured copper IOs show promising superhydrophilic behaviors with most of the time regimes. However, in the process of nanostructuring, the pores and necks of copper IOs are partly filled by those nanostructures, this might decrease the nanostructured copper IOs' permeability. To minimize this, we can either increase the neck size of the copper IOs before nanostructuring or decrease nanofeatures' size. The latter option is further investigated in section 3.5.

3.5 Copper IOs with Nanoneedles (Solution B1)

As noted in section 2.3.1, an increase in solution temperature decreases the nanostructure size by dissolving the nanoflowers and nanograsses, leaving behind the small nanoneedles (0.3 μm). To fabricate nanoneedles on copper IO surfaces, the immersion time is varied up to 1 min to

avoid over-oxidation since the copper IOs possess much higher surface area than polished copper plates and hence exhibit a faster rate of oxidation.

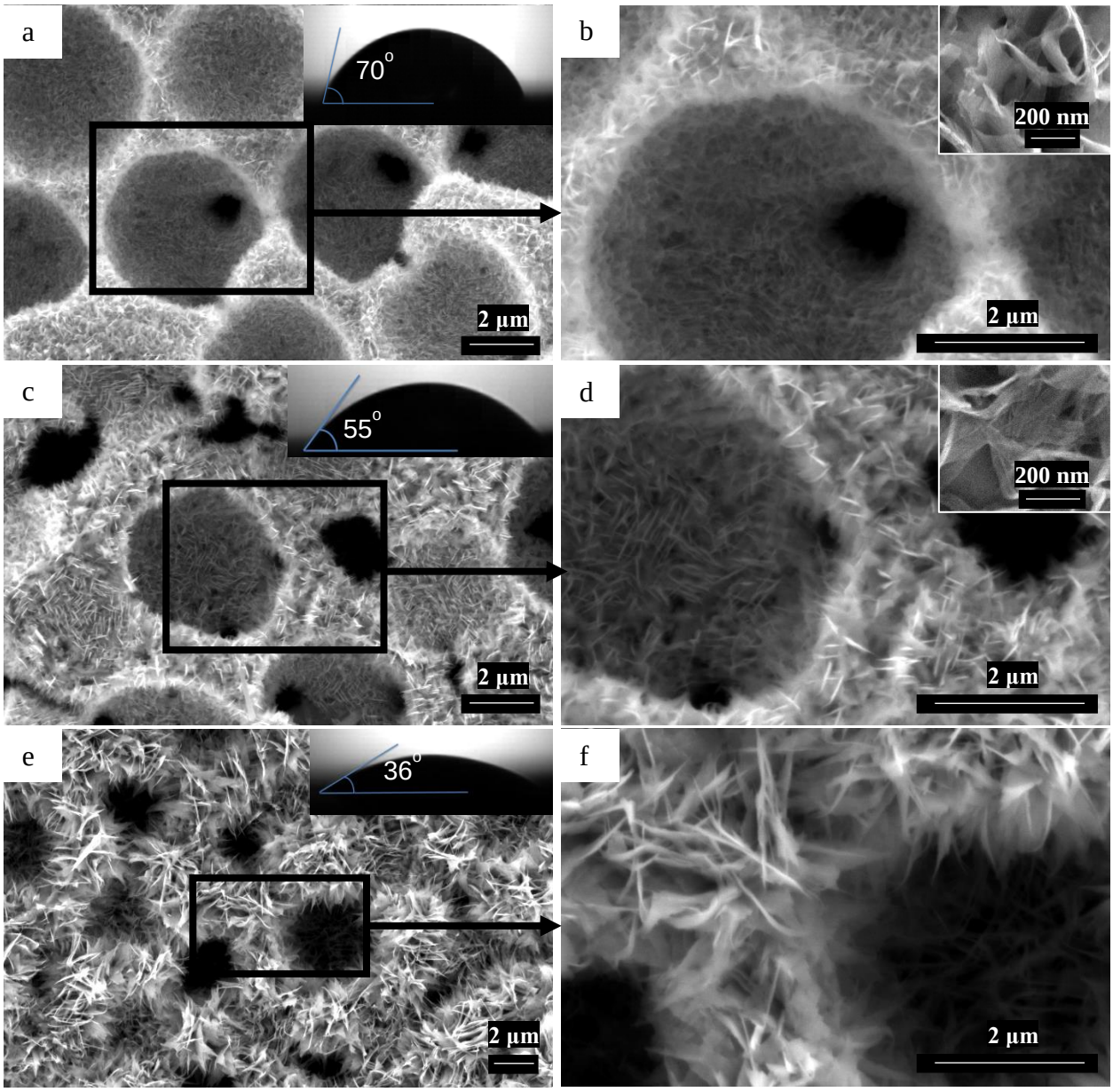

Figure 3.6 SEM images of copper IOs studded with nanoneedles fabricated by solution immersion for (a,b) 15 secs, (c,d) 20 secs, and (e,f) 1 min. Insets of a,c, and e show static CAs on respective surfaces. Insets of b and d show close-up views of nanoneedles.

Consequently, figure 3.6a, c, and e show the SEM images of copper IOs decorated with nanoneedles for the immersion time of 15 secs, 20 secs, and 1 min with the respective static CAs

in insets. A magnified view of the nanoneedles at 15 secs (figure 3.6b inset) and 20 secs (figure 3.6d inset) immersion presents the morphology of nanoneedles which are sharp nanobelts with multiple bends. With an increase in immersion time, the nanoneedle length increases from ~ 0.24 μm to 1.96 μm and CAs decrease from 70^o to 36^o. However, nanostructures within copper IOs start clogging interconnecting pores of IOs as shown in figure 3.6e and f. To minimize the clogging effects, we can limit the oxidation time to 20 secs to preserve pore diameters with the demonstration of desired hydrophilicity (CA=55^o).

In conclusion, we discuss how to create hierarchical porous copper by combining copper IOs and solution immersion methods in order to improve interfacial surface area which can be used in thermal wicking materials. With the demonstration of nanostructures within copper IOs, the IO surfaces exhibit superhydrophilicity (from hydrophobicity) by decreasing their CAs. Since the nanostructuring process using solution immersion methods is an additive process, it is important to investigate the volumetric change via nanostructure construction to minimize the clogging of interconnected pores.

CHAPTER 4: CONCLUDING REMARKS

4.1 Summary

In summary, we have successfully fabricated various nanostructures (*i.e.* nanoflakes, nanoflowers, nanograsses, nanoneedles, nanotrenches, and nanomesh) on bare copper substrates and porous copper structures by controlling solution immersion methods parameters (*i.e.* chemical composition, immersion time, and solution temperature). Then, we measure the contact angles of fabricated samples to quantify their wetting characteristics with varying nanostructures. In this process, we capture the top view SEM images and cross-sectional view FIB-SEM images to reconstruct the three-dimensional topological maps of copper oxide nanostructures. This enables to compute nanostructures' morphological parameters (*i.e.* sizes, shapes, and number density) and surface roughness (from the three-dimensional topography). The morphological details and surface chemical contents are used to understand their effects on water CAs based on the Wenzel theory. In general, the combination of surface roughness and surface oxides improves the hydrophilicity of nanostructured copper with increasing chemical immersion time. This study will allow us to systemically design nanostructures on copper substrates with desired wetting characteristics.

4.2 Challenges and Future Work

The interfacial properties of sessile droplets' interfaces are known to strongly depend on surface-active impurities and nanostructure variations across the sample[53]. Therefore, it is critical to reduce the number of surface impurities and concomitantly improve nanostructure uniformity in order to provide consistent wetting properties. To address this issue, we will carefully handle impurities in the future work where the potential impurity sources are listed below:

- Improper pre- and post-fabrication cleaning can increase organic surface impurities.

- A long exposure to NaOH solution (t > 30 mins) can induce Na compound residues on surfaces (figure 4.1a)
- Improper polishing before chemical immersion can create deep scratches on copper surfaces, which act as nanostructure nucleation sites (figure 4.1b). This can be minimized through a uniform polishing using sandpapers (220 to 1200 grits).

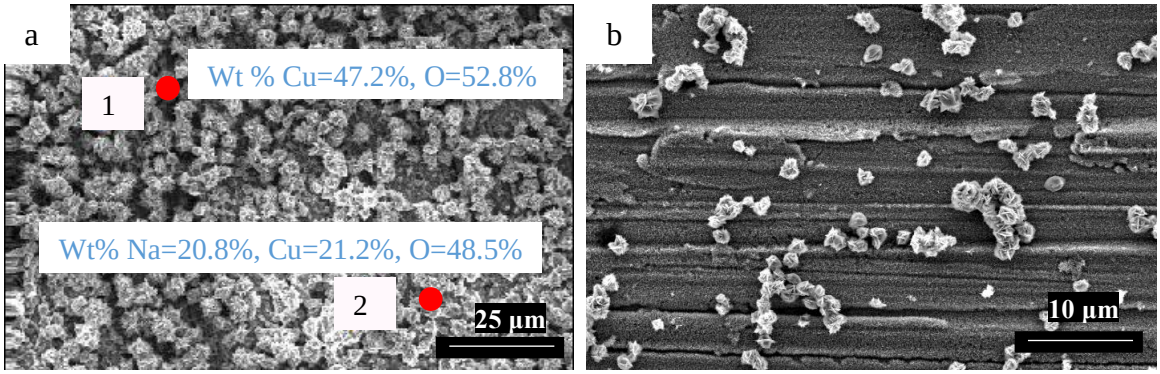

Figure 4.1 (a) Na compound residues are confirmed using EDS analysis (bottom) among copper oxide nanoflowers (top). (b) Scratches on improperly polished samples act as nanoflowers' nucleation sites.

In future study, we plan to further investigate the nanostructures' morphological parameters in addition to nanostructures' size, shape, number density, and roughness. The further parameters include (1) oxide layer thickness in order to understand the volumetric portion of copper and copper oxide after the solution immersion; (2) based on the copper oxide layer thickness, it is critical to quantify the updated neck size and corresponding structural porosity; and (3) uniformity and conformity of copper oxide nanostructures across the sample (lateral direction) and through the sample thickness (vertical direction).

Another challenge will be associated with an analysis that quantifies surface chemical composition. During chemical composition analysis using the GIXRD method, the grazing angle is 0.3^{o} to the sample surface. This causes the X-rays to penetrate up to a depth of 1 µm, providing us a sub-surface chemical composition rather than a surface chemical composition. Accurate

chemistry characterization can be addressed by employing advanced surface chemistry analysis such as X-ray photoelectron spectroscopy (XPS) in the future.

Concluding Remarks

In this research, we have investigated the fabrication methods to demonstrate nanostructured copper substrates and porous copper with hydrophilic properties in order to improve fluid transport properties. This research will provide a systematic understanding of the design parameters of heterogeneous nanostructured copper so as to directly control their wetting characteristics. This research can pave the way to fabricate hydrophilic nanostructured surfaces for their potential use in thermofluidic applications.

REFERENCES

(1) Chowdhuri, A.; Gupta, V.; Sreenivas, K.; Kumar, R.; Mozumdar, S.; Patanjali, P. K. Response Speed of SnO_2-Based H_2S Gas Sensors with CuO Nanoparticles. *Appl. Phys. Lett.* **2004**, *84* (7), 1180–1182 DOI: 10.1063/1.1646760.

(2) Zhou, K.; Wang, R.; Xu, B.; Li, Y. Synthesis, Characterization and Catalytic Properties of CuO Nanocrystals with Various Shapes. *Nanotechnology* **2006**, *17* (15), 3939–3943 DOI: 10.1088/0957-4484/17/15/055.

(3) Sung, W.; Kim, W.; Lee, S.; Lee, H.; Kim, Y.; Park, K.; Lee, S. Field Emission Characteristics of CuO Nanowires by Hydrogen Plasma Treatment. *Vacuum* **2007**, *81*, 851–856 DOI: 10.1016/j.vacuum.2006.10.002.

(4) Wang, S.; Liu, K.; Yao, X.; Jiang, L. Bioinspired Surfaces with Superwettability: New Insight on Theory, Design, and Applications. *Chem. Rev.* **2015**, *115* (16), 8230–8293 DOI: 10.1021/cr400083y.

(5) Zhang, Q.; Zhang, K.; Xu, D.; Yang, G.; Huang, H.; Nie, F.; Liu, C.; Yang, S. CuO Nanostructures: Synthesis, Characterization, Growth Mechanisms, Fundamental Properties, and Applications. *Prog. Mater. Sci.* **2014**, *60* (1), 208–237 DOI: 10.1016/j.pmatsci.2013.09.003.

(6) Im, Y.; Dietz, C.; Lee, S. S.; Joshi, Y. Flower-Like CuO Nanostructures for Enhanced Boiling. *Nanoscale Microscale Thermophys. Eng.* **2012**, *16* (3), 145–153 DOI: 10.1080/15567265.2012.678564.

(7) Liu, J.; Huang, X.; Li, Y.; Sulieman, K. M.; He, X.; Sun, F. Hierarchical Nanostructures of Cupric Oxide on a Copper Substrate: Controllable Morphology and Wettability. *J. Mater.*

Chem. **2006**, *16* (45), 4427 DOI: 10.1039/b611691d.

(8) Kulinich, S. A.; Farhadi, S.; Nose, K.; Du, X. W. Superhydrophobic Surfaces: Are They Really Ice-Repellent? *Langmuir* **2011**, *27* (1), 25–29 DOI: 10.1021/la104277q.

(9) Drelich, J.; Chibowski, E.; Meng, D. D.; Terpilowski, K. Hydrophilic and Superhydrophilic Surfaces and Materials. *Soft Matter* **2011**, *7* (21), 9804 DOI: 10.1039/c1sm05849e.

(10) Kong, L.-H.; Chen, X.-H.; Yu, L.-G.; Wu, Z.-S.; Zhang, P.-Y. Superhydrophobic Cuprous Oxide Nanostructures on Phosphor-Copper Meshes and Their Oil–Water Separation and Oil Spill Cleanup. *ACS Appl. Mater. Interfaces* **2015**, *7* (4), 2616–2625 DOI: 10.1021/am507620s.

(11) Dorri, N.; Shahbazi, P.; Kiani, A. Self-Movement of Water Droplet at the Gradient Nanostructure of Cu Fabricated Using Bipolar Electrochemistry. *Langmuir* **2014**, *30* (5), 1376–1382 DOI: 10.1021/la403566b.

(12) Alheshibri, M. H.; Rogers, N. G.; Sommers, A. D.; Eid, K. F. Spontaneous Movement of Water Droplets on Patterned Cu and Al Surfaces with Wedge-Shaped Gradients. *Appl. Phys. Lett.* **2013**, *102* (17) DOI: 10.1063/1.4802926.

(13) Seo, J.; Lee, S.-K.; Lee, J.; Seung Lee, J.; Kwon, H.; Cho, S.-W.; Ahn, J.-H.; Lee, T. Path-Programmable Water Droplet Manipulations on an Adhesion Controlled Superhydrophobic Surface. *Sci. Rep.* **2015**, *5*, 12326 DOI: 10.1038/srep12326.

(14) Young, T. An Essay on the Cohesion of Fluids. *Philos. Trans. R. Soc. London* **1805**, *95* (0), 65–87 DOI: 10.1098/rstl.1805.0005.

(15) Wenzel, R. N. Resistance of Solid Surfaces. *Ind. Eng. Chem.* **1936**, *28*, 988–994 DOI:

10.1021/ie50320a024.

(16) Cassie, A. B. D.; Baxter, S. Wettability of Porous Surfaces,. *Trans. Faraday Soc.* **1944**, *40* (5), 546–551.

(17) Marmur, A.; Bittoun, E. When Wenzel and Cassie Are Right: Reconciling Local and Global Considerations. *Langmuir* **2009**, *25* (3), 1277–1281 DOI: 10.1021/la802667b.

(18) Meiron, T. S.; Marmur, A.; Saguy, I. S. Contact Angle Measurement on Rough Surfaces. *J. Colloid Interface Sci.* **2004**, *274* (2), 637–644 DOI: 10.1016/j.jcis.2004.02.036.

(19) Kim, P.; Kreder, M. J.; Alvarenga, J.; Aizenberg, J. Hierarchical or Not? Effect of the Length Scale and Hierarchy of the Surface Roughness on Omniphobicity of Lubricant-Infused Substrates. *Nano Lett.* **2013**, *13* (4), 1793–1799 DOI: 10.1021/nl4003969.

(20) Zou, Y.; Li, Y.; Zhang, N.; Liu, X. Flower-like CuO Synthesized by CTAB-Assisted Hydrothermal Method. *Bull. Mater. Sci.* **2011**, *34* (4), 967–971 DOI: 10.1007/s12034-011-0223-0.

(21) Eskandari, A.; Sangpour, P.; Vaezi, M. R. Hydrophilic Cu_2O Nanostructured Thin Films Prepared by Facile Spin Coating Method: Investigation of Surface Energy and Roughness. *Mater. Chem. Phys.* **2014**, *147* (3), 1204–1209 DOI: 10.1016/j.matchemphys.2014.07.008.

(22) Xu, X.; Yang, H.; Liu, Y. Self-Assembled Structures of CuO Primary Crystals Synthesized from $Cu(CH_3COO)_2$–NaOH Aqueous Systems. *CrystEngComm* **2012**, *14* (16), 5289 DOI: 10.1039/c2ce25420d.

(23) Leu, D.-J. H. and T.-S. Fabrication of a Wettability-Gradient Surface on Copper by Screen-Printing Techniques. *J. Micromechanics Microengineering* **2015**, *25* (8), 85007 DOI:

10.1088/0960-1317/25/8/085007.

(24) Nam, Y.; Ju, Y. S. Fabrication and Characterization of Superhydrophilic Cu Microposts for Micro Heat Pipes. In *Proceedings of PowerMEMS 2009*; 2009; pp 123–126.

(25) Miljkovic, N.; Enright, R.; Nam, Y.; Lopez, K.; Dou, N.; Sack, J.; Wang, E. N. Jumping-Droplet-Enhanced Condensation on Scalable Superhydrophobic Nanostructured Surfaces. *Nano Lett.* **2013**, *13* (1), 179–187 DOI: 10.1021/nl303835d.

(26) Wang, S.; Feng, L.; Jiang, L. One-Step Solution-Immersion Process for the Fabrication of Stable Bionic Superhydrophobic Surfaces. *Adv. Mater.* **2006**, *18* (6), 767–770 DOI: 10.1002/adma.200501794.

(27) He, Z.; He, J.; Zhang, Z. Selective Growth of Metallic Nanostructures on Microstructured Copper Substrate in Solution. *CrystEngComm* **2015**, *17* (38), 7262–7269 DOI: 10.1039/C5CE01093D.

(28) Huang, D.; Leu, T. Applied Surface Science Fabrication of High Wettability Gradient on Copper Substrate. *Appl. Surf. Sci.* **2013**, *280*, 25–32 DOI: 10.1016/j.apsusc.2013.04.065.

(29) Cabrera, N.; Mott, N. F. Theory of the Oxidation of Metals. *Reports Prog. Phys.* **1949**, *12* (1), 308 DOI: 10.1088/0034-4885/12/1/308.

(30) Zhou, G.; Wang, L.; Yang, J. C. Effects of Surface Topology on the Formation of Oxide Islands on Cu Surfaces. *J. Appl. Phys.* **2005**, *97* (6), 2841–233115 DOI: 10.1063/1.1861147.

(31) Kratohvil, S.; Matijevic, E. Preparation of Copper-Compounds of Different Compositions and Particle Morphologies. *J. Mater. Res.* **1991**, *6* (4), 766–777 DOI: 10.1557/JMR.1991.0766.

(32) Gattinoni, C.; Michaelides, A. Atomistic Details of Oxide Surfaces and Surface Oxidation: The Example of Copper and Its Oxides. *Surf. Sci. Rep.* **2015** DOI: 10.1016/j.surfrep.2015.07.001.

(33) Anžel, I. High Temperature Oxidation of Metals and Alloys. *Metal. Metall.* **2000**, 325–336.

(34) Nam, Y.; Ju, Y. S. Comparative Study of Copper Oxidation Schemes and Their Effects on Surface Wettability. In *Volume 10: Heat Transfer, Fluid Flows, and Thermal Systems, Parts A, B, and C*; ASME, 2008; pp 1833–1838.

(35) Chaudhary, A.; Barshilia, H. C. Nanometric Multiscale Rough $CuO/Cu(OH)_2$ Superhydrophobic Surfaces Prepared by a Facile One-Step Solution-Immersion Process: Transition to Superhydrophilicity with Oxygen Plasma Treatment. *J. Phys. Chem. C* **2011**, *115* (37), 18213–18220 DOI: 10.1021/jp204439c.

(36) Yin, S.; Wu, D.; Yang, J.; Lei, S.; Kuang, T.; Zhu, B. Fabrication and Surface Characterization of Biomimic Superhydrophobic Copper Surface by Solution-Immersion and Self-Assembly. *Appl. Surf. Sci.* **2011**, *257* (20), 8481–8485 DOI: 10.1016/j.apsusc.2011.04.137.

(37) Pei, M.-D.; Wang, B.; Li, E.; Zhang, X.; Song, X.; Yan, H. The Fabrication of Superhydrophobic Copper Films by a Low-Pressure-Oxidation Method. *Appl. Surf. Sci.* **2010**, *256* (20), 5824–5827 DOI: 10.1016/j.apsusc.2010.03.039.

(38) Zhang, W.; Wen, X.; Yang, S. Controlled Reactions on a Copper Surface: Synthesis and Characterization of Nanostructured Copper Compound Films. *Inorg. Chem.* **2003**, *42* (16), 5005–5014 DOI: 10.1021/ic0344214.

(39) Lee, J.-Y.; Han, J.; Lee, J.; Ji, S.; Yeo, J.-S. Hierarchical Nanoflowers on Nanograss Structure for a Non-Wettable Surface and a SERS Substrate. *Nanoscale Res. Lett.* **2015**, *10* (1), 505 DOI: 10.1186/s11671-015-1214-7.

(40) Boshkovikj, V.; Webb, H. K.; Pham, V. T.; Fluke, C. J.; Crawford, R. J.; Ivanova, E. P. Three-Dimensional Reconstruction of Surface Nanoarchitecture from Two-Dimensional Datasets. *AMB Express* **2014**, *4* (1), 3 DOI: 10.1186/2191-0855-4-3.

(41) Tabet, M. F.; Urban, F. K. Comparison of Atomic Force Microscope and Rutherford Backscattering Spectrometry Data of Nanometre Size Zinc Islands. *Thin Solid Films* **1996**, *290–291*, 312–316 DOI: 10.1016/S0040-6090(96)08968-7.

(42) Kerber, S. J.; Barr, T. L.; Mann, G. P.; Brantley, W. A.; Papazoglou, E.; Mitchell, J. C. The Complementary Nature of X-Ray Photoelectron Spectroscopy and Angle-Resolved X-Ray Diffraction Part I : Background and Theory. *J. Mater. Eng. Perform.* **1998**, *7* (June), 329–333 DOI: 10.1361/105994998770347765.

(43) Zhang, W.; Wen, X.; Yang, S. Controlled Reactions on a Copper Surface: Synthesis and Characterization of Nanostructured Copper Compound Films. *Inorg. Chem.* **2003**, *42* (16), 5005–5014 DOI: 10.1021/ic0344214.

(44) Cheng, J.; Sun, Y. F.; Zhao, A.; Huang, Z. H.; Xu, S. P. Preparation of Gradient Wettability Surface by Anodization Depositing Copper Hydroxide on Copper Surface. *Trans. Nonferrous Met. Soc. China (English Ed.)* **2015**, *25* (7), 2301–2307 DOI: 10.1016/S1003-6326(15)63845-6.

(45) Feng, J.; Qin, Z.; Yao, S. Factors Affecting the Spontaneous Motion of Condensate Drops on Superhydrophobic Copper Surfaces. *Langmuir* **2012**, *28* (14), 6067–6075 DOI:

10.1021/la300609f.

(46) Zhang, C.; Lingamneni, S.; Barako, M. T.; Palko, J. W.; Asheghi, M.; Goodson, K. E. Characterization of the Capillary Performance of Copper Inverse Opals. In *Proceedings of the 15th InterSociety Conference on Thermal and Thermomechanical Phenomena in Electronic Systems, ITherm 2016*; 2016; pp 1035–1039.

(47) Liu, Q.; Tang, Y.; Luo, W.; Fu, T.; Yuan, W. Fabrication of Superhydrophilic Surface on Copper Substrate by Electrochemical Deposition and Sintering Process. *Chinese J. Chem. Eng.* **2015**, *23* (7), 1200–1205 DOI: 10.1016/j.cjche.2014.11.034.

(48) Deng, D.; Wan, W.; Xie, Y.; Huang, Q.; Chen, X. Fabrication of Porous Copper Surfaces by Laser Micromilling and Their Wetting Properties. *Precis. Eng.* **2017**, *49*, 428–439 DOI: 10.1016/j.precisioneng.2017.04.005.

(49) Zhang, C.; Rong, G.; Palko, J. W.; Dusseault, T. J.; Asheghi, M.; Santiago, J. G.; Goodson, K. E. Tailoring of Permeability in Copper Inverse Opal for Electronic Cooling Applications. In *ASME 2015 International Technical Conference and Exhibition on Packaging and Integration of Electronic and Photonic Microsystems collocated with the ASME 2015 13th International Conference on Nanochannels, Microchannels, and Minichannels*; ASME, 2015.

(50) Colson, P.; Henrist, C.; Cloots, R. Nanosphere Lithography: A Powerful Method for the Controlled Manufacturing of Nanomaterials. *J. Nanomater.* **2013**, *2013*, 1–19 DOI: 10.1155/2013/948510.

(51) Won, Y.; Barako, M. T.; Agonafer, D. D.; Asheghi, M.; Goodson, K. E. Mechanical and Thermal Properties of Copper Inverse Opals for Two-Phase Convection Enhancement. In

Thermomechanical Phenomena in Electronic Systems -Proceedings of the Intersociety Conference; 2014; pp 326–332.

(52) Washburn, E. W. The Dynamics of Capillary Flow. *Phys. Rev.* **1921**, *17* (3), 273–283 DOI: 10.1103/PhysRev.17.273.

(53) Ponce-Torres, A.; Vega, E. J.; Montanero, J. M. Effects of Surface - Active Impurities on the Liquid Bridge Dynamics. *Exp. Fluids* **2016**, *57* (5), 67 1-12 DOI: 10.1007/s00348-016-2152-6.

(54) Liu, J.; Huang, X.; Li, Y.; Li, Z.; Chi, Q.; Li, G. Formation of Hierarchical CuO Microcabbages as Stable Bionic Superhydrophobic Materials via a Room-Temperature Solution-Immersion Process. *Solid State Sci.* **2008**, *10* (11), 1568–1576 DOI: 10.1016/j.solidstatesciences.2008.02.005.

(55) Guo, Z.-G.; Fang, J.; Hao, J.; Liang, Y.; Liu, W. A Novel Approach to Stable Superhydrophobic Surfaces. *ChemPhysChem* **2006**, *7* (8), 1674–1677 DOI: 10.1002/cphc.200600217.

(56) Zeng, O.; Wang, X.; Yuan, Z.; Wang, M.; Huang, J. Fabrication of a Superhydrophobic Surface on Copper Foil Based on Ammonium Bicarbonate and Paraffin Wax Coating. *Surf. Topogr. Metrol. Prop.* **2015**, *3* (3), 35001 DOI: 10.1088/2051-672X/3/3/035001.

(57) Chen, X.; Kong, L.; Dong, D.; Yang, G.; Yu, L.; Chen, J.; Zhang, P. Synthesis and Characterization of Superhydrophobic Functionalized $Cu(OH)_2$ Nanotube Arrays on Copper Foil. *Appl. Surf. Sci.* **2009**, *255* (7), 4015–4019 DOI: 10.1016/j.apsusc.2008.10.104.

(58) Zhang, N.; Lu, S.; Xu, W.; Zhang, Y. Controlled Growth of CuO–Cu_3Pt/Cu Micro-Nano

Binary Architectures on Copper Substrate and Its Superhydrophobic Behavior. *New J. Chem. New J. Chem* **2014**, *4534* (38), 4534–4540 DOI: 10.1039/c4nj00660g.

(59) Chen, X.; Kong, L.; Dong, D.; Yang, G.; Yu, L.; Chenand, J.; Zhang, P. Fabrication of Functionalized Copper Compound Hierarchical Structure with Bionic Superhydrophobic Properties. *J. Phys. Chem. C* **2009**, *113* (14), 5396–5401 DOI: 10.1021/jp809616d.

(60) Huang, D. J.; Leu, T. S. Fabrication of High Wettability Gradient on Copper Substrate. *Appl. Surf. Sci.* **2013**, *280*, 25–32 DOI: 10.1016/j.apsusc.2013.04.065.

(61) Wang, G.; Zhang, T.-Y. Easy Route to the Wettability Cycling of Copper Surface between Superhydrophobicity and Superhydrophilicity. *ACS Appl. Mater. Interfaces* **2012**, *4* (1), 273–279 DOI: 10.1021/am2013129.